

1
2 Fourth-order hybrid phase field analysis with non-equal order elements
3 and dual meshes for simulating crack propagation
4

5 Feng Zhu^a, Hongxiang Tang^{a, *}, Xue Zhang^b, George Papazafeiropoulos^c

6
7 ^aState Key Laboratory of Coastal and Offshore Engineering, Dalian University of

8 Technology, 116023 Dalian, China

9 ^bDepartment of Civil Engineering and Industrial Design

10 University of Liverpool, Liverpool, L69 3BX, UK

11 ^cInstitute of Structural Analysis and Antiseismic Research, National Technical University of

12 Athens // Zografou Campus, Athens 15780, Greece

13
14 * Corresponding author.

15 Tel.: +86-411-84708511-807

16 E-mail address: tanghx@dlut.edu.cn

19 **Abstract:** High computational cost handicaps the practical application of the phase
20 field approach for rock-like materials. The aim of this study was to investigate the
21 feasibility of saving computing resources, especially computing time, by reducing the
22 number and order of displacement elements. Specifically, we developed a novel scheme
23 (i.e., TMNE) based on dual meshes and non-equal order elements using NURBS-based
24 IGA, and then combined it with the hybrid formulation of the fourth-order model to
25 tackle the high computing cost. The scheme was shown to save more than 50% of the
26 computing time and the number of DOFs compared with the traditional scheme in most
27 cases. This indicates that there is a possibility of wasting computing resources in
28 traditional discretization of displacement field. Additionally, the scheme simplifies the
29 data transfer between meshes and only one case need to be considered, even when
30 combined with adaptive remeshing. Last but not least, the scheme can also be extended
31 to a variety of NURBS elements (C^0 - C^4) as required.

32

33 **Keywords:** hybrid formulation, phase field model, NURBS, Isogeometric analysis,
34 dual meshes, rock-like materials

35

36

37

38 **1. Introduction**

39 Fracture is detrimental to the mechanical properties of many engineering materials,
40 such as rock-like materials, concrete, metal, etc., and thus the stability of engineering
41 structures. It also contributes to health problems when occurring in living tissues and
42 artificial implants inside human bodies. Research on fracture is therefore of significant
43 importance in many engineering cases (Ambati et al., 2014; Wu et al., 2020; Zhu and
44 Zhao, 2021), and it also contribute to the development of advanced composites and
45 understanding physiological processes of tissues and organs (Gao et al., 2021; Meng et
46 al., 2018).

47 Numerical modelling is a powerful tool for studying fracture, particularly when the
48 physical tests are high-cost or the full-scale tests are unfeasibility. Indeed, numerical
49 modelling may provide detailed information on the evolution process of fracture and
50 crack propagation and thus give useful clues to researchers on the mechanism of
51 fracture related failure problems.

52 In general, numerical methods for simulating fracture can be roughly divided into
53 two categories, namely discontinuum mechanics and continuum mechanics. Typical
54 discontinuum mechanics that are widely used include, but are not limited to, the
55 molecular dynamics method (Bauchy et al., 2015; Ebrahim et al., 2018), the discrete
56 element method (Orozco et al., 2019; Suchorzewski et al., 2018), etc. The continuum
57 mechanics can be further classified into local and non-local continuum mechanics. For

58 non-local continuum mechanics, the peridynamics proposed by Silling et al.(Silling,
59 2000; Silling et al., 2007) is one of the most representative approaches. A typical feature
60 is an integral equation instead of a partial differential equation, which thus provides a
61 unified mechanical framework for discrete particles, continuous media and continuous
62 media with evolving discontinuities. As a result, peridynamics is widely applied in
63 geotechnical engineering. For example, Song (Menon and Song, 2019) applied their
64 proposed state-based peridynamic hydromechanical framework to simulate desiccation
65 cracking in unsaturated soils, thereby providing a new insight into the mechanical
66 properties of desiccation cracking. Subsequently, Song et al. (Menon and Song, 2021)
67 extended the stable coupled periporomechanics model proposed in (Menon and Song,
68 2021a) to unguided cracking problems in unsaturated porous media, based on the
69 effective force state concept in (Song and Silling, 2020). In terms of computation
70 efficiency, Han Fei et al (Wang et al., 2021) recently presented a hybrid peridynamics
71 and classical continuum mechanics modeling approach, where peridynamics is
72 adaptively activated in the region of reaching material strength. In addition, as stated in
73 (Menon and Song, 2021b; Song and Khalili, 2019; Song and Menon, 2019),
74 peridynamics is also suitable for simulating local progressive failure in unsaturated
75 soils. As for local continuum mechanics (i.e., classical continuum mechanics), it can be
76 subdivided into discrete type and smeared type depending on the crack representation.
77 The discrete type attempts to capture the exact topology of crack surfaces either in an
78 explicit way, such as CZM (Salih et al., 2016), or in an implicit manner, such as XFEM
79 (Gao et al., 2019; Ghandriz et al., 2020). Mesh dependence in many cases is the issue

80 associated with the method for an explicit representation of fracture topology as crack
81 can only propagates along mesh edges. In contrast, the implicit version, such as the
82 XFEM, does not have this issue; it is however still not competitive when handling
83 cracking of complexity such as multiple cracks and crack coalescence and branching.
84 Readers are referred to (Rabczuk, 2013) for more details on this aspect. The smeared
85 methods no longer capture the exact topology of crack surfaces, but smear the discrete
86 crack to a finite width through a continuous scalar field. Thereby they convert the
87 discrete crack propagation into a continuous problem. Among them, the phase field
88 approach (Borden, 2012; Borden et al., 2012; Bourdin et al., 2000; Miehe et al., 2010;
89 Nguyen et al., 2020) is a representative smeared method which has been attracting
90 increasing attentions.

91 The phase field approach, as a mathematical model for interfacial problems, has
92 been applied to handle numerous challenging problem such as fracture (Bourdin et al.,
93 2000; Goswami et al., 2019; Miehe et al., 2010; Nguyen et al., 2020), hydrogen
94 embrittlement (Huang and Gao, 2020) , solidification (Boettinger et al., 2002; Yu et al.,
95 2018), vesicle dynamics (Biben et al., 2005), and viscous fingering (Nguyen et al.,
96 2010). For fracture, there are two basic versions of the phase field model which were
97 from the physics and mechanics communities, respectively (Ambati et al., 2014). The
98 model from the physics community is derived by adapting the phase transition
99 formalism of Landau and Ginzburg (Franklin, 1916), whereas the model from the
100 mechanics community originates from the regularization of a variational principle of

101 brittle fracture (Bourdin et al., 2000; Francfort and Marigo, 1998). The latter is
102 concerned in this study and thus, if not otherwise specified, the phase field method is
103 referred to the one from mechanics community in the following. Smearing an actual
104 crack to a finite width using a damage variable ϕ , the crack propagation problem with
105 discontinuity is reformulated as a standard continuous multi-field problem in the phase
106 field modelling. As demonstrated, the phase field method can simulate crack
107 propagation in complex fracture networks where crack coalescence and branching may
108 take place forthrightly without imposing any additional ad-hoc criteria. Its extension
109 from 2D cases to 3D cases is also straightforward. Due to its appealing features, the
110 phase field has been attracting increasing attentions and used successfully for various
111 fracture problems such as brittle fracture (Borden et al., 2016, 2014; Chen et al., 2020;
112 Zhang et al., 2017a), dynamic fracture (Borden et al., 2012; Ren et al., 2019), ductile
113 fracture (Ambati et al., 2016, 2015; Huang and Gao, 2019), multi-field fracture (Ni et
114 al., 2020), cohesive fracture (Geelen et al., 2019; Remacle et al., 2012), fracture in thin
115 shells (Amiri et al., 2014), rubbery polymers (Miehe and Schänzel, 2014) and
116 composites (Zhang et al., 2021), etc. Similarly, the phase field model is also widely
117 used in geotechnical engineering. For example, Zhang et al. (Zhang et al., 2017a)
118 proposed a modified phase-field model for rock-like materials which can distinguish
119 between the critical energy release rates for mode I and mode II cracks. Fei and Choo
120 (Fei and Choo, 2020) present a novel phase-field model of shear fracture in pressure-
121 sensitive geomaterials which is capable of properly capturing the effect of friction in
122 the fracture propagation mechanism.

123 Despite its advantages in handling cracking problems, the phase field is associated
124 with high computational cost which handicaps its applications. The high computational
125 cost is mainly ascribed to the facts that (1) an extremely fine mesh in the local damage
126 area is required to obtain a stable crack propagation, and (2) the convergence rate of the
127 commonly used staggered scheme is low. To reduce the computational cost, the
128 commonly used technologies include, but are not limited to, the adaptive remeshing
129 (Goswami et al., 2020b; Hirshikesh et al., 2019, 2021; Muixí et al., 2020; Paul et al.,
130 2020), the parallel computing (Hirshikesh et al., 2021), the dual-mesh scheme
131 (Goswami et al., 2019; Hu et al., 2009) and their combination. Among them, Goswami
132 et al. (2019) pioneered the use of a dual-mesh scheme in the hybrid formulation of the
133 second-order model to study the brittle crack propagation. In the scheme, both the
134 displacement field and damage field employ PHT-splines, and an adaptive h-refinement
135 is carried out based on their respective refinement strategies. It is shown (Goswami et
136 al., 2019) that the dual-mesh scheme can significantly reduce the computational cost
137 while ensuring the accuracy. Nevertheless, in the dual-mesh scheme proposed in
138 (Goswami et al., 2019), the correspondence between the meshes for displacement and
139 damage fields is not fixed which results in the complexity for variable mapping between
140 the two meshes. Additionally, though PHT-Splines possesses the excellent properties of
141 local refinement, it can only use a bicubic C^1 element in many cases (Deng et al., 2008;
142 Li et al., 2010). This higher-order element, which exceeds the requirements of the phase
143 field approach, and its reduced regularity (Vuong et al., 2011) are likely to waste some
144 computing resources.

145 Inspired by the pioneering works of Goswami et al. (2019), the authors developed
146 a novel scheme (TMNE) based on the NURBS-based IGA (Hughes et al., 2005; Tang
147 et al., 2021; Vázquez, 2016; Zhu et al., 2021) and the hybrid formulation of the fourth-
148 order model (Ambati et al., 2014; Borden et al., 2014; Goswami et al., 2020b, 2019)
149 for modelling crack propagation and associated failure phenomena in rock-like
150 materials. The TMNE scheme can be summarized as NURBS-based **Two Meshes** and
151 **Non-Equal** order elements, where the displacement field adopts a coarser mesh and
152 bilinear C^0 NURBS elements, while the damage field adopts a finer mesh and
153 biquadratic C^1 NURBS elements. The novelty of this work is twofold:

154 (1) Dual meshes and non-equal order elements are adopted in this manuscript to
155 reduce the computing time. The number of elements used for the displacement field is
156 1/4 of that for the damage field in 2D cases and 1/8 in 3D case (For more details, please
157 see Section 3.3 and Figs. 4 and 7). The examples show that both the non-equal order
158 elements and the dual meshes can reduce the computing time by more than 30%, while
159 the TMNE can reduce the computing time and the number of DOFs by more than 50%
160 in most cases.

161 (2) The TMNE scheme simplifies the data transfer between meshes and only one
162 case need to be considered, even when combined with adaptive remeshing, because the
163 correspondence relationship between two meshes is fixed.

164 The remainder of the paper is structured as follows: Section 2 briefly outlines the
165 hybrid formulation of the fourth-order phase field, including the governing equations,

166 strain energy decomposition, and hybrid-staggered solution scheme. The corresponding
 167 isogeometric discretization are presented in the Section 3. Furthermore, this section also
 168 gives a detailed introduction to the TMNE scheme, such as the principle of TMNE, the
 169 data transmission, and the algorithm flowchart. Section 4 illustrates the computational
 170 advantages of the TMNE scheme in the phase field approach through six representative
 171 examples. Finally, some conclusions and future research directions are given in Section
 172 5.

173 **2. Phase-field formulation**

174 This section briefly presents the formulation of the fourth-order phase field in the
 175 hybrid-staggered scheme (Ambati et al., 2014; Borden et al., 2014; Goswami et al.,
 176 2020b, 2019). The phase field model in mechanics community was derived from the
 177 variational formulation of brittle fracture by Francfort and Marigo (Francfort and
 178 Marigo, 1998) and the regularization by Bourdin et al. (Bourdin et al., 2000). In the
 179 model, the crack propagation is assumed to be the competition between the stored bulk
 180 energy and the crack surface energy. Under a quasi-static condition, the total energy
 181 functional \mathcal{E} of the phase field model is expressed as follows:

$$182 \quad \mathcal{E} = \Psi_s + \Psi_c - \mathcal{P}_{\text{external}} \quad (1)$$

183 where Ψ_s is the stored bulk energy, Ψ_c indicates the crack surface energy, and
 184 $\mathcal{P}_{\text{external}}$ represents the external potential energy. Specifically, they are defined as

$$185 \quad \Psi_s(\mathbf{u}, \phi) = \int_{\Omega} \Psi(\boldsymbol{\varepsilon}(\mathbf{u}), \phi) d\Omega \quad (2)$$

186
$$\Psi(\boldsymbol{\varepsilon}(\mathbf{u}), \phi) = g(\phi) \Psi_0(\boldsymbol{\varepsilon}) \quad (3)$$

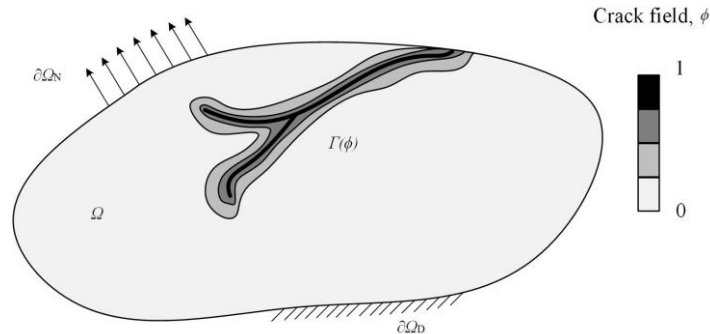
187
$$\Psi_0(\boldsymbol{\varepsilon}) = \frac{1}{2} \boldsymbol{\varepsilon}^T C_0 \boldsymbol{\varepsilon} = \frac{1}{2} \boldsymbol{\varepsilon}^T \boldsymbol{\sigma}_0 \quad (4)$$

188
$$\Psi_c(\phi) = \int_{\Omega} G_c \Gamma_{\phi, n}(\phi) d\Omega \quad (5)$$

189
$$\mathcal{P}_{\text{external}}(\mathbf{u}) = \int_{\Omega} \mathbf{b} \cdot \mathbf{u} d\Omega + \int_{\partial\Omega_N} \mathbf{t}_N \cdot \mathbf{u} d\Gamma \quad (6)$$

190 where Ω represents the computational domain (see also Fig.1), $\Psi(\boldsymbol{\varepsilon}(\mathbf{u}), \phi)$ refers to
 191 the energy storage function, $\Psi_0(\boldsymbol{\varepsilon})$ is the elastic strain energy density, $g(\phi)$ is a
 192 monotonically decreasing stress-degradation function, C_0 is the linear elastic stiffness
 193 matrix, $\boldsymbol{\varepsilon}$ is the strain tensor, G_c is the critical energy release rate, $\Gamma_{\phi, n}$ is the crack
 194 surface density functional, \mathbf{b} is the distributed force acting on the computational
 195 domain Ω , \mathbf{t}_N is the traction applied over the Neumann boundary $\partial\Omega_N$, and the vector
 196 \mathbf{u} is the displacement. The critical energy release rate, G_c , is a constant depending on
 197 the material itself, while $\Gamma_{\phi, n}$ relies on the length-scale parameter L_c , the phase field
 198 ϕ and its derivatives. The length-scale parameter L_c governs the amount of diffusion
 199 of the crack, and for $L_c \rightarrow 0$ the sharp crack case is approached.

200



201

202 Fig. 1. A solid body Ω with the approximated diffuse crack bands $\Gamma(\phi)$

203 2.1 Fourth-order phase field theory

204 The fourth-order phase field model requires its shape function of at least C^1
205 continuity due to the high-order derivative of ϕ in PDE. Therefore, the fourth-order
206 model is usually only applied to higher-order numerical methods such as IGA (Garau
207 and Vázquez, 2018; Hughes et al., 2005; Tang et al., 2021; Zhu et al., 2021), meshfree
208 methods (Chen et al., 2017), etc. Comparing to the second-order model, the fourth-
209 order model requires less degrees of freedom to maintain the accuracy of modelling.
210 Additionally, the higher-order derivatives strengthen the regularity of the crack
211 description and, thereby, significantly improves the convergence rate and calculation
212 accuracy of the numerical approximations (Borden et al., 2014). Readers are referred
213 to (Borden et al., 2014) for more detailed information related to the forth-order phase
214 field model. In this study, the crack surface energy $\Psi_c(\phi)$ of the fourth-order model
215 used in (Borden et al., 2014) is employed:

$$216 \quad \Psi_c(\phi) = \int_{\Gamma} G_c d\Gamma \approx \int_{\Omega} G_c \Gamma_{\phi,4} d\Omega \quad (7)$$

217 where the crack surface density functional $\Gamma_{\phi,4}$ of phase-field variable, ϕ , is defined
218 as

$$219 \quad \Gamma_{\phi,4} = \frac{\phi^2}{2L_c} + \frac{L_c}{4} (\nabla(\phi))^2 + \frac{L_c}{32} (\Delta\phi)^2 \quad (8)$$

220 2.2 Energy decomposition

221 In the phase field model, the stored bulk energy Ψ_s describes a smooth transition
222 from the intact bulk material to the fully crack state, characterized by the elastic strain

223 energy density $\Psi_0(\boldsymbol{\varepsilon})$ and a stress-degradation function $g(\phi)$. Bourdin et al. (2000)
 224 indicated that the crack evolution equation based on Eq. (3) cannot distinguish between
 225 fracture behaviors in tension and compression, which may cause the model to produce
 226 unphysical crack patterns under a compression state. To overcome this issue, the elastic
 227 strain energy density $\Psi_0(\boldsymbol{\varepsilon})$ is decomposed into a tension part Ψ_0^+ and a compression
 228 part Ψ_0^- following (Miehe et al., 2010)

$$229 \quad \Psi_0^\pm = \frac{\lambda \langle \text{tr}[\boldsymbol{\varepsilon}] \rangle_\pm^2}{2} + \mu \text{tr}[\boldsymbol{\varepsilon}_\pm^2] \quad (9)$$

230 where λ and μ are the *lamé* constants. The expressions of $\boldsymbol{\varepsilon}_+$ and $\boldsymbol{\varepsilon}_-$ are

$$231 \quad \boldsymbol{\varepsilon}_+ = \sum_{l=1}^3 \langle \varepsilon_l \rangle_+ \mathbf{n}_l \otimes \mathbf{n}_l, \quad \boldsymbol{\varepsilon}_- = \sum_{l=1}^3 \langle \varepsilon_l \rangle_- \mathbf{n}_l \otimes \mathbf{n}_l \quad (10)$$

232 with bracket operators $\langle x \rangle_+ := (x + |x|)/2$ and $\langle x \rangle_- := (x - |x|)/2$. ε_l and \mathbf{n}_l are
 233 the eigenvalue and eigenvector of strain, respectively. Using the above definition, the
 234 stored bulk energy Ψ_s (i.e., Eq. (2)) is rewritten as

$$235 \quad \Psi_s(\mathbf{u}, \phi) = \int_{\Omega} \Psi(\boldsymbol{\varepsilon}(\mathbf{u}), \phi) d\Omega, \quad \Psi(\boldsymbol{\varepsilon}(\mathbf{u}), \phi) = g(\phi) \Psi_0^+(\boldsymbol{\varepsilon}) + \Psi_0^-(\boldsymbol{\varepsilon}) \quad (11)$$

236 As such, $g(\phi)$ only acts on $\Psi_0^+(\boldsymbol{\varepsilon})$ in Eq. (11), implying that only the elastic strain
 237 energy density corresponding to the tension component is degraded.

238 2.3 Hybrid-staggered scheme

239 The phase field model treats the displacement field and the damage field (or phase
 240 field) as the basic fields. These two fields may be solved via either a monolithic or
 241 staggered scheme, where, respectively, the two unknown fields are solved
 242 simultaneously or alternately.

243 Although the traditional monolithic scheme is more efficient, it may encounter
244 convergence issue when unstable crack propagation occurs. However, Goswami et al.
245 (Goswami et al., 2020a) recently pioneered a new physics informed neural network
246 algorithm called VE-PINN by minimizing the variational energy. In fact, VE-PINN has
247 opened up a new paradigm for using modern neural network architectures to solve the
248 fracture problems. This new monolithic scheme can not only deal with the unstable
249 crack propagation, but also significantly reduce the number of “elements”. Even in
250 some examples (Goswami et al., 2020c), the incremental step size can be enlarged by
251 100-1000 times compared with the staggered scheme(Goswami et al., 2019; Miehe et
252 al., 2010). Subsequently, using the Bezier operator, Goswami et al. (Goswami et al.,
253 2020c) extend it to adaptive h-refinement framework to achieve local domain
254 refinement along the flow of the crack. For more information, please refer to the review
255 paper (Samaniego et al., 2020) and chapters 5 and 6 of the doctoral dissertation
256 (Goswami, 2020). However, as stated (Goswami et al., 2021a), the bottleneck of VE-
257 PINN is that independent simulations are required to perform for every different input
258 parameters, computing domain, or boundary conditions. To overcome this fundamental
259 challenge, the paper (Goswami et al., 2021b) proposed a variational energy-based
260 framework of DeepONet. Once trained, this model can predict the fracture path and
261 corresponding displacement at any position of the crack tip and under any applied load
262 within a fraction of a second.

263 On the other hand, the staggered scheme may handle unstable crack propagation.
 264 It is, however, more computationally intensive and requires a time increment sensitivity
 265 study. In view of this, a hybrid-staggered scheme proposed in (Ambati et al., 2014) is
 266 adopted in this study. It is shown that the hybrid-staggered scheme (Ambati et al., 2014;
 267 Goswami et al., 2019) ensures the robustness in dealing with unstable crack propagation.
 268 Meanwhile, its computational cost is one order of magnitude lower than the traditional
 269 staggered scheme.

270 In the hybrid model, the equilibrium equation is derived from the isotropic model
 271 (Bourdin et al., 2000), whereas the phase field evolution equation is based on the
 272 anisotropic model (Miehe et al., 2010). Specifically, the equilibrium equation is

$$273 \quad -\nabla \cdot g(\phi)\boldsymbol{\sigma} = \mathbf{f} \quad (12)$$

274 in which no energy decomposition is considered. The phase field evolution equation is
 275 expressed as

$$276 \quad G_c \left[\frac{\phi}{L_c} - \frac{L_c}{2} |\nabla\phi|^2 + \frac{L_c}{16} \Delta^2 \phi \right] = -g'(\phi)H(\mathbf{x},t) \quad (13)$$

277 where $H(\mathbf{x},t)$ is a history-field variable defined as

$$278 \quad H(\mathbf{x},t) = \max_{t \in [t_0, t_n]} \Psi_0(\boldsymbol{\varepsilon}(\mathbf{x},t)) \quad (14)$$

279 As shown in Eq. (13), $H(\mathbf{x},t)$ is the maximum positive strain energy at integration
 280 point \mathbf{x} from the initial time t_0 to the current time t_n .

281 **3. NURBS-based IGA and TMNE scheme**

282 *3.1 A brief introduction of NURBS*

283 In this section, the characteristics of NURBS is briefly reviewed. An in-depth
 284 introduction to the NURBS can be found in (Piegl and Tiller, 1997). A NURBS curve,
 285 \mathbf{C}_N , of order p can be expressed as

286
$$\mathbf{C}_N = \sum_{i=1}^m N_{i,p}(\xi) \mathbf{P}_i \quad (15)$$

287 where m is the number of control points, \mathbf{P}_i is the coordinates, and $N_{i,p}$ represents
 288 the univariate NURBS shape function in the form

289
$$N_{i,p}(\xi) = \frac{\mathbf{B}_{i,p}(\xi)w_i}{\sum_{k=1}^m \mathbf{B}_{k,p}(\xi)w_k} \quad (16)$$

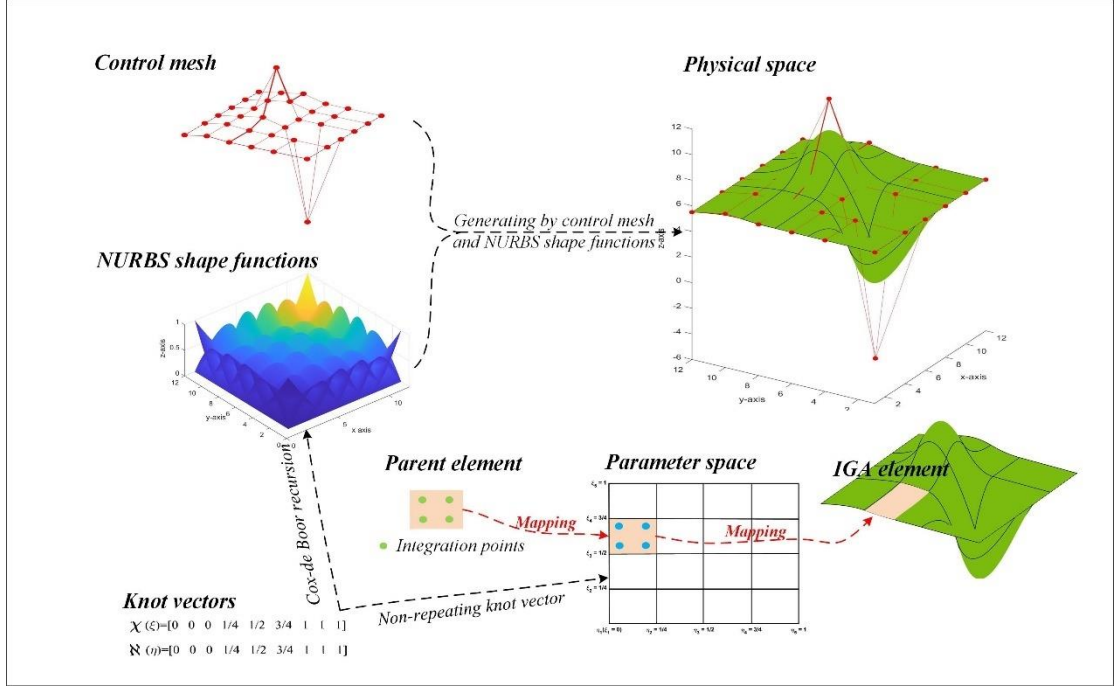
290 where w_i is a set of non-negative weights, and $\mathbf{B}_{i,p}$ is the univariate B-spline
 291 function determined by the Cox-de Boor recursion formula (Piegl and Tiller, 1997) and
 292 an open, non-decreasing knot vector $\mathbf{E} = [\xi_1, \xi_2, \dots, \xi_{n+p+1}]$. According to (Piegl and
 293 Tiller, 1997), a NURBS surface, $\mathbf{S}_N(\xi, \eta)$, of order p in ξ -direction and order q in
 294 η -direction can be expressed as follows:

295
$$\mathbf{S}_N(\xi, \eta) = \sum_{i=1}^m \sum_{j=1}^n N_{i,j}^{p,q}(\xi, \eta) \mathbf{P}_{i,j} \quad (17)$$

296 The bivariate NURBS shape function $N_{i,j}^{p,q}(\xi, \eta)$ in Eq. (17) can be written as

297
$$N_{i,j}^{p,q}(\xi, \eta) = \frac{\mathbf{B}_{i,p}(\xi)\mathbf{B}_{j,q}(\eta)w_{i,j}}{\sum_{k=1}^m \sum_{l=1}^n \mathbf{B}_{k,p}(\xi)\mathbf{B}_{l,q}(\eta)w_{k,l}} \quad (18)$$

298 Fig.2 shows a NURBS surface, the NURBS shape functions and IGA elements, and the
 299 control mesh composed of control points (similar to FEA nodes). However, due to the
 300 tensor product of NURBS, this manuscript adopts a uniformly refined mesh.



301

302 Fig. 2. Schematic illustration of NURBS-based IGA: knot vectors, NURBS shape
 303 functions, control mesh constructed by control points, a NURBS surface, parametric
 304 space, and IGA elements.

305 3.2 Spatial discretization of the fourth-order model

306 The weak form formulations of the fourth-order model can be expressed as follows:

$$307 \begin{cases} \int_{\Omega} \{\boldsymbol{\sigma} \delta \boldsymbol{\varepsilon} - \mathbf{b} \cdot \delta \mathbf{u}\} d\Omega - \int_{\partial\Omega_N} \mathbf{t}_N \cdot \delta \mathbf{u} d\Omega_N = 0 \\ \int_{\Omega} \left\{ G_c \left[\frac{1}{L_c} \phi \delta \phi + \frac{L_c}{2} \nabla \phi \cdot \nabla \delta \phi + \frac{L_c}{16} \Delta \phi \cdot \Delta \delta \phi \right] + g'(\phi) H \delta \phi \right\} d\Omega = 0 \end{cases} \quad (19)$$

308 Using the NURBS shape function, the displacement field \mathbf{u} and the damage field ϕ
 309 are discretized as

$$310 \quad \mathbf{u} = \sum_{i=1}^m N_i^u \mathbf{u}_i, \quad \phi = \sum_{j=1}^n N_j^\phi \phi_j \quad (20)$$

311 where the shape function matrix N_i^u and the vector \mathbf{u}_i are defined as

$$312 \quad N_i^u = \begin{bmatrix} N_i & 0 \\ 0 & N_i \end{bmatrix}, \quad \mathbf{u}_i = \begin{bmatrix} u_x \\ u_y \end{bmatrix} \quad (21)$$

313 In Eq. (20), we have $m \neq n$ due to the use of different elements for the two fields.

314 N_j^ϕ and ϕ_j possess similar form as these in Eq. (21). Consequently, the associated

315 derivatives can be defined as

$$316 \quad \boldsymbol{\varepsilon} = \sum_{i=1}^m \mathbf{B}_i^{\mathbf{u}} \mathbf{u}_i, \quad \nabla \phi = \sum_{j=1}^n \mathbf{B}_j^\phi \phi_j, \quad \Delta \phi = \sum_{j=1}^n \mathbf{D}_j^\phi \phi_j \quad (22)$$

317 where $\boldsymbol{\varepsilon} = [\varepsilon_{xx}, \varepsilon_{yy}, \varepsilon_{xy}]^T$, and the related matrices are

$$318 \quad \mathbf{B}_i^{\mathbf{u}} = \begin{bmatrix} N_{i,x} & 0 \\ 0 & N_{i,y} \\ N_{i,y} & N_{i,x} \end{bmatrix}, \quad \mathbf{B}_j^\phi = \begin{bmatrix} N_{j,x} \\ N_{j,y} \end{bmatrix}, \quad \mathbf{D}_j^\phi = N_{j,xx} + N_{j,yy} \quad (23)$$

319 Similarly, the variations of \mathbf{u} and ϕ and their derivatives can be discretized as

$$320 \quad \begin{cases} \delta \mathbf{u} = \sum_{i=1}^m N_i^{\mathbf{u}} \delta \mathbf{u}_i, & \Delta \delta \phi = \sum_{j=1}^n \mathbf{D}_j^\phi \delta \phi_j, & \delta \phi = \sum_{j=1}^n N_j^\phi \delta \phi_j \\ \delta \boldsymbol{\varepsilon} = \sum_{i=1}^m \mathbf{B}_i^{\mathbf{u}} \delta \mathbf{u}_i, & \nabla \delta \phi = \sum_{j=1}^n \mathbf{B}_j^\phi \delta \phi_j, & \Delta \delta \phi = \sum_{j=1}^n \mathbf{D}_j^\phi \delta \phi_j \end{cases} \quad (24)$$

321 Using the approximated variables (i.e., Eqs. (20)-(24)) and the weak form of the

322 governing equations (i.e., Eq.(19)), the residual for the displacement field, $\mathbf{R}_i^{\mathbf{u}}$ and

323 the damage field, \mathbf{R}_j^ϕ are as follow:

$$324 \quad \begin{cases} \mathbf{R}_i^{\mathbf{u}} = \int_{\Omega} g(\phi) (\mathbf{B}_i^{\mathbf{u}})^T \boldsymbol{\sigma} d\Omega - \int_{\partial\Omega_N} (N_i^{\mathbf{u}})^T \mathbf{t}_N d\Omega_N - \int_{\partial\Omega} (N_i^{\mathbf{u}})^T \mathbf{b} d\Omega = 0 \\ \mathbf{R}_j^\phi = \int_{\Omega} \left\{ G_c \left[\frac{1}{L_c} N_j \phi + \frac{L_c}{2} (\mathbf{B}_j^\phi)^T \nabla \phi + \frac{L_c}{16} \mathbf{D}_j^\phi \Delta \phi \right] + g'(\phi) H N_j \right\} d\Omega = 0 \end{cases} \quad (25)$$

325 Employing the Newton-Raphson method, the following algebraic equations can be

326 obtained

$$327 \quad \begin{bmatrix} \mathbf{K}^{\mathbf{u}\mathbf{u}} & 0 \\ 0 & \mathbf{K}^{\phi\phi} \end{bmatrix} \begin{Bmatrix} d\mathbf{u} \\ d\phi \end{Bmatrix} = \begin{Bmatrix} \mathbf{F}^{\mathbf{u}} \\ \mathbf{F}^{\phi} \end{Bmatrix} \quad (26)$$

328 where $\mathbf{K}^{\mathbf{u}\mathbf{u}}$ and $\mathbf{K}^{\phi\phi}$ are written as

$$329 \quad \begin{cases} \mathbf{K}_{ik}^{\mathbf{u}\mathbf{u}} = \frac{\partial \mathbf{R}_i^{\mathbf{u}}}{\partial \mathbf{u}_k} = \int_{\Omega} g(\phi) (\mathbf{B}_i^{\mathbf{u}})^T C_e \mathbf{B}_k^{\mathbf{u}} d\Omega \\ \mathbf{K}_{jl}^{\phi\phi} = \frac{\partial \mathbf{R}_j^\phi}{\partial \phi_l} = \int_{\Omega} \left\{ G_c \left[\left(\frac{1}{L_c} + 2H \right) N_j N_l + \frac{L_c}{2} (\mathbf{B}_j^\phi)^T \mathbf{B}_l^\phi + \frac{L_c}{16} \mathbf{D}_j^\phi \mathbf{D}_l^\phi \right] \right\} d\Omega \end{cases} \quad (27)$$

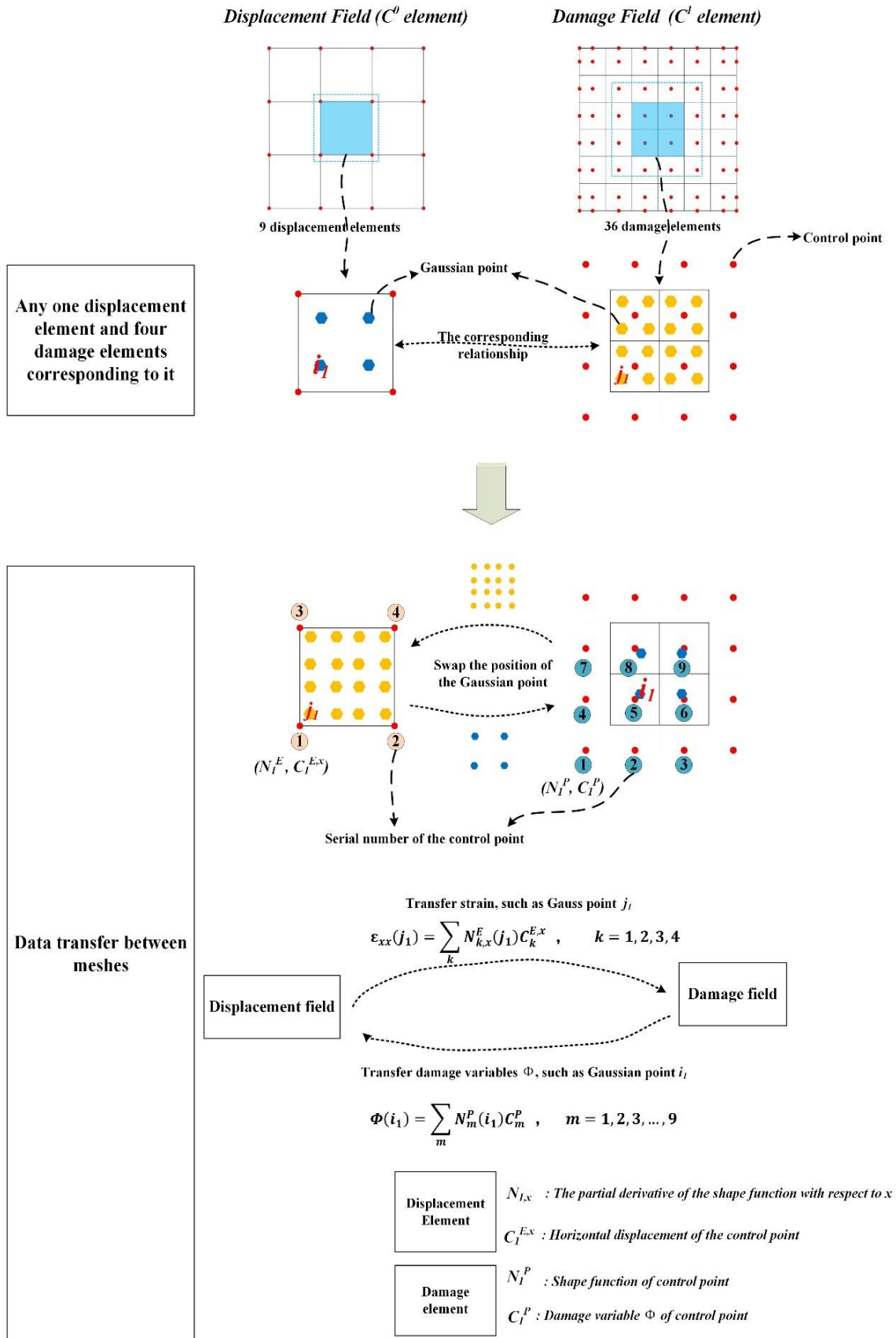
343 More specifically, the containment relationship between the displacement element
344 and the damage element is fixed, and the number of elements used for the displacement
345 field is 1/4 of that for the damage field in 2D cases (1/8 in 3D cases). This kind of spatial
346 discretization is mainly based on the following three reasons :

347 a) According to the pioneering work of (Goswami et al., 2019), the optimal balance
348 between calculation accuracy and computational cost seems to be that the damage
349 element size is taken as 1/2 of the displacement element. Namely, the number of
350 elements used for the displacement field is 1/4 of that for the damage field in 2D
351 cases and 1/8 in 3D cases.

352 b) The authors adopt 2×2 Gaussian points in both the displacement element and the
353 damage element. In the process of transferring data between meshes, each
354 displacement element contains 4 damage elements, that is, 16 damage integration
355 points; each corresponding damage element contains a displacement integration
356 point, as depicted in Figs. 4 and 7. When the displacement field transfers the strain
357 to the damage field to update the historical variables driving the crack propagation,
358 only the first partial derivative of the displacement shape function at these 16
359 damage integration points needs to be calculated. Similarly, when the damage field
360 transfers damage variables to the displacement field to characterize the degradation
361 of the stiffness matrix, only the value of the damage shape function at this
362 displacement integration point needs to be computed. Then, multiply and
363 accumulate these values with the corresponding element node (or control point)

364 variables to realize data transfer between meshes (see Figs. 4 and 7). In short, data
365 transfer can be achieved by exchanging the integration points of the two fields.
366 This method is not only simple and easy to implement, but also has no errors.

367 c) In addition, another purpose is to hope that even when combined with adaptive
368 remeshing, the containment relationship between displacement and damage
369 elements remains fixed. In this way, data transfer between meshes is easy to
370 implement, and only one case needs to be considered. Otherwise, if the
371 containment relationship is not fixed, it is first necessary to determine which
372 damaged elements a given displacement element contains, or which displacement
373 element a given damaged element belongs to; Then, data transfer can be achieved
374 by exchanging Gaussian points. This process may lead to several situations. Of
375 course, the latter method is more in line with the actual situation and will have
376 higher calculation accuracy. However, as mentioned earlier, one of our goals in
377 proposing TMNE is to hope that it can be easily implemented.

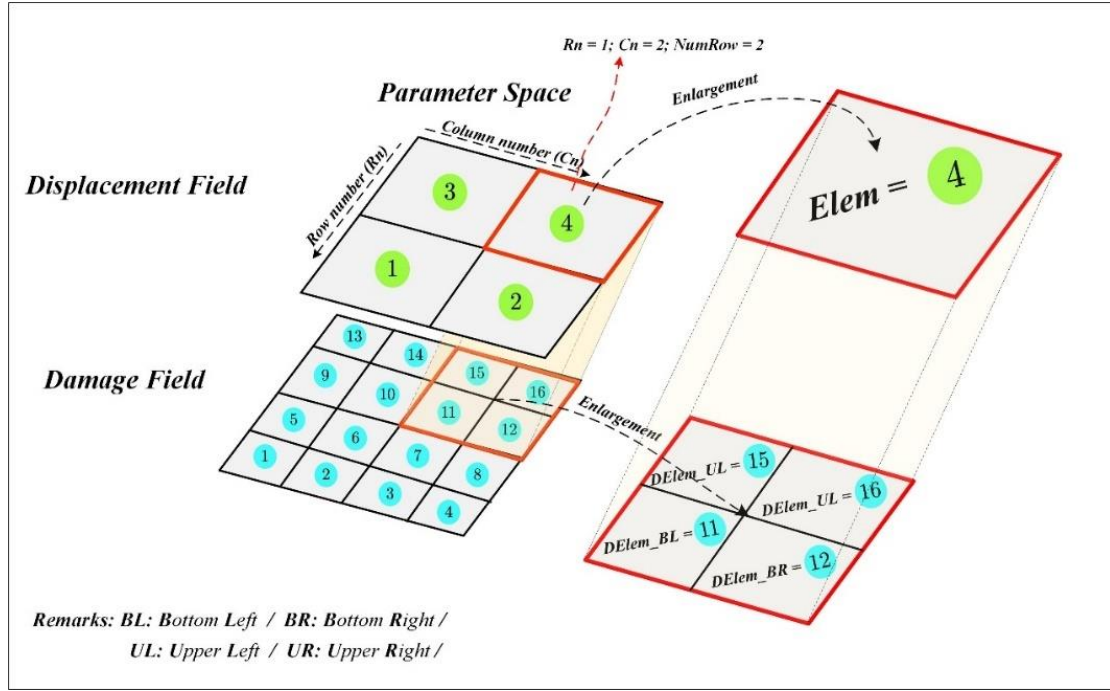


378

379 Fig. 4. Schematic illustration of the principle of data transfer between meshes

380 3.4 Data transmission

381 The TMNE scheme requires data transfer between two meshes in each iteration.
382 Specifically, the strain tensor $\boldsymbol{\varepsilon}$ has to be calculated based on the displacement field
383 and transferred to the damage field in each iteration to compute the driving force for
384 crack propagation. The damage scalar ϕ needs to be transferred to characterize the
385 degradation of material stiffness for solving the displacement field. To simplify the
386 implementation of the data transfer, the parameter space (as plotted in Fig. 3) of IGA
387 is employed. In IGA, the parameter space is generated by non-repeated knots in the
388 knot vectors, while the elements are obtained by mapping the parameter space to the
389 physical space (as depicted in Figs. 2 and 3). Consequently, regardless of the
390 complexity of the configuration of the physical space, the parameter space is always a
391 simple square mesh. According to this and inspired by the pioneering works of Borden
392 et al.(Borden et al., 2014), Ambati et al.(Ambati et al., 2014), and Goswami et al.
393 (Goswami et al., 2019), a relational array *MeshArrays* and two function spaces
394 *DispDamageSpace* and *DamageDispSpace* are constructed for data transfer between
395 meshes in this study. Compared with the data transfer in (Goswami et al., 2019), this
396 method reduces a relational array.



397

398

Fig. 5. Topological relationship between coarse and fine meshes

399

The relational array *MeshArrays* is a *NumDispElem* × 4 matrix (see Table 1) used

400

to store the topological relationship between two meshes. In *MeshArrays*, the row

401

number refers to the displacement element's number, and the four elements in each row

402

are the numbers of the corresponding damage elements. This array can be easily

403

obtained (see also Fig. 5) as

404

$$\begin{cases} DElem_{BR} = 4(Elem - Cn) + 2Cn \\ DElem_{BL} = DElem_{BR} - 1 \\ DElem_{UL} = DElem_{BL} + 2NumRow \\ DElem_{UR} = DElem_{BR} + 2NumRow \end{cases} \quad (28)$$

405

where, in the parameter space, *Elem* is the number of the displacement element, *C_n* is

406

its column, and *NumRow* is the number of elements in each row.

407

408 **Table 1**

409 Definition of some variables

Name	Definition
<i>NumDispElem</i>	The number of elements in the displacement field
<i>NumDispControl</i>	The number of control points in a displacement element
<i>NumDispInteg</i>	The number of integration points in a displacement element
<i>NumDamageElem</i>	The number of elements in the damage field
<i>NumDamageControl</i>	The number of control points in a damage element
<i>NumDamageInteg</i>	The number of integration points in a damage element

410

411 *DispDamageSpace* is a $NumDispElem \times 2NumDispControl \times NumDamageInteg$

412 array (see Table 1) and refers to the function space that transfers the strain ϵ from the

413 displacement field to the damage field (as depicted on the right side of Fig. 7).

414 Whereas *DamageDispSpace* is a $NumDamageElem \times NumDamageControl \times$

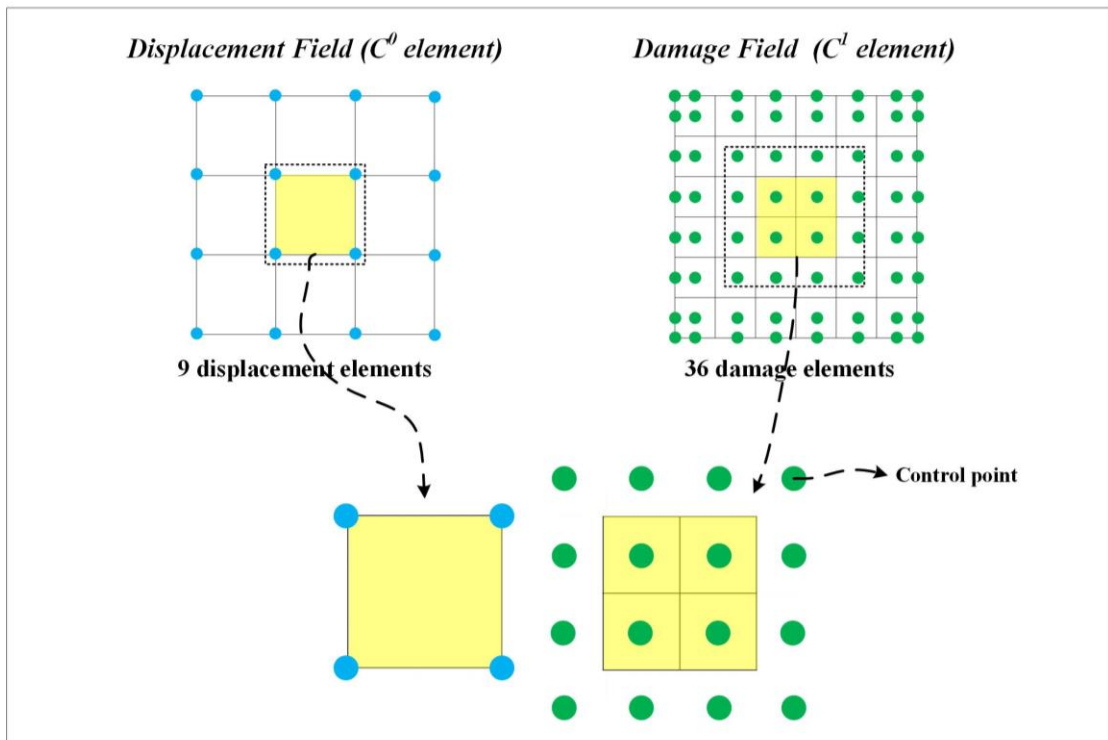
415 $NumDispInteg$ array (see Table 1) and indicates the function space that transfers the

416 damage variable ϕ from the damage field to the displacement field (as plotted on the

417 left side of Fig. 7). Among them, the representative elements in Fig. 7 is taken as the

418 middle position of the computational domain, as plotted in Fig. 6. In fact, as

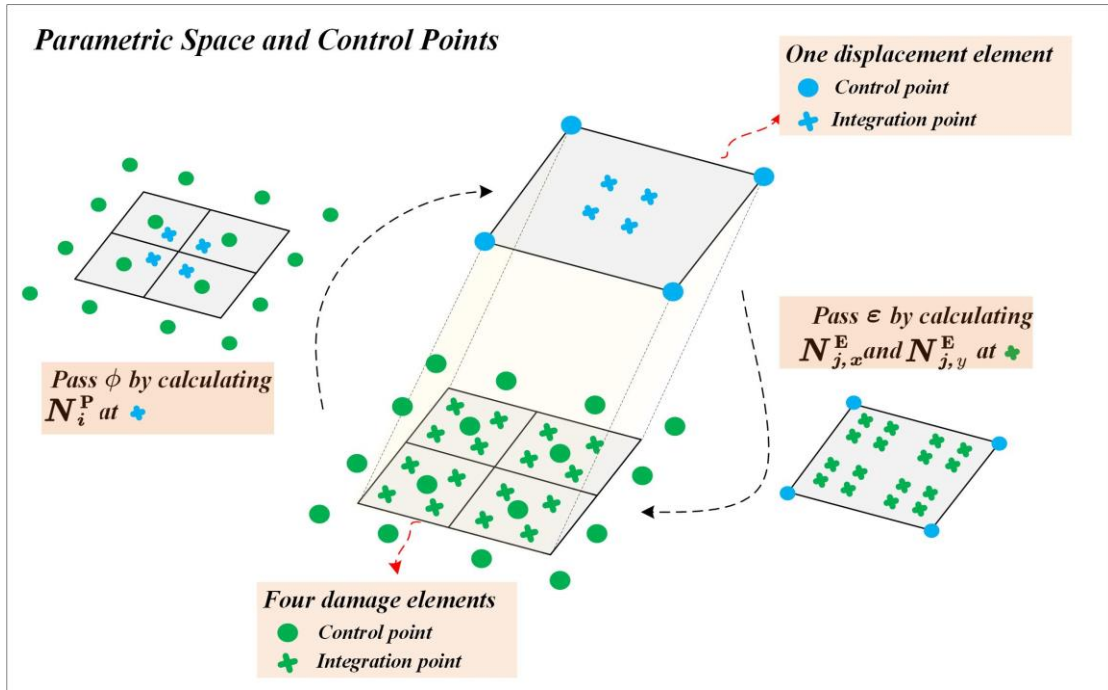
419 mentioned in section 3.3 above, data transfer can be achieved by exchanging the
 420 integration points of the two fields. In addition, using the tensor product of NURBS,
 421 the calculation of the 2-D (or 3-D) shape function value can be decomposed into two
 422 (or three) 1-D shape functions, and then the 1-D shape function values are assembled
 423 accordingly. This method not only saves computational time, but also facilitates
 424 numerical implementation. Fig. 8 shows the process of constructing
 425 *DamageDispSpace* according to this method, and the construction of
 426 *DispDamageSpace* is similar to this.



427

428 Fig. 6. Location of the representative element in the computational domain

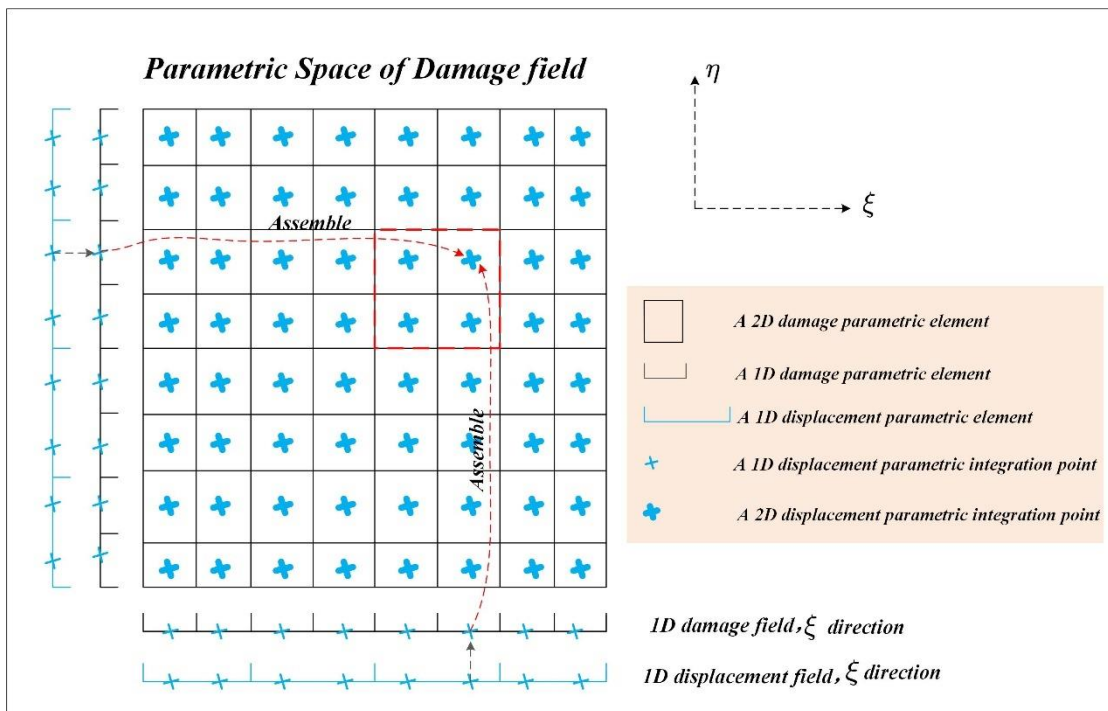
429



430

431

Fig. 7. Function space for data transfer between meshes



432

433

Fig. 8. Calculate the damage shape function at the displacement integration point

434

through 1-D assembly

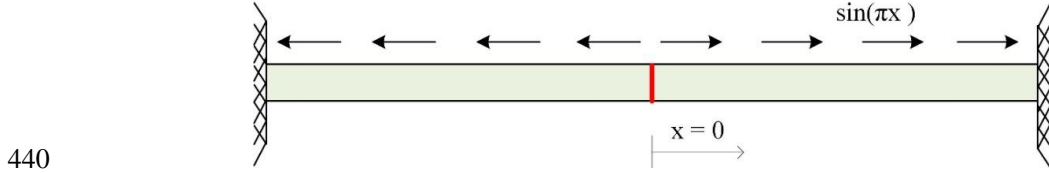
435 3.5 The algorithm flowchart.

436 The key steps of the proposed TMNE scheme for simulating crack propagation
437 are outlined as follows:

1. Calculate the function spaces (i.e., *DispSpace*, *DamageSpace*, *DispDamageSpace*, and *DamageDispSpace*) and the relational array (i.e., *MeshArrays*).
2. Loop over time steps (e.g., time step $t + \Delta t$)
 - a) Loop over iterations (e.g., the i th iteration)
 - i. Calculate the displacement stiffness matrix K_i^{uu} and the right term r_i^u by calling *DispSpace*, *DamageDispSpace* and ϕ_i .
 - ii. Calculate nodal displacement u_{i+1} , $u_{i+1} = (K_i^{uu})^{-1} r_i^u$
 - iii. Calculate the damage stiffness matrix $K_i^{\phi\phi}$ and the right term r_i^ϕ by calling *DamageSpace*, *DispDamageSpace* and u_{i+1} .
 - iv. Calculate nodal damage ϕ_{i+1} , $\phi_{i+1} = (K_i^{\phi\phi})^{-1} r_i^\phi$
 - v. $i \leftarrow i + 1$
 - vi. Check for convergence
3. Repeat the loop for the next time step until the calculation is complete.

438 **4. Numerical examples**

439 *4.1 One-dimensional model*



441 Fig. 9. One-dimensional model of a bar with a centered crack

442 We first verify the proposed TMNE scheme against a one-dimensional problem
 443 (Goswami et al., 2019; Schillinger et al., 2015) for which the analytical solution is
 444 available. The schematic diagram of the model is shown in Fig. 9. The bar clamped on
 445 both sides has an initial vertical penetrating crack in the middle and is subject to a
 446 sinusoidal load. For simplicity, the Young's modulus is $E = 1$, the cross-sectional area
 447 is $A = 1$, and the strain $\boldsymbol{\varepsilon}$ in the fracture zone is assumed to be non-negative. Thus,
 448 the stress-strain relationship of the one-dimensional bar can be defined as follows:

449
$$\boldsymbol{\sigma} = g(\phi)\boldsymbol{\varepsilon} \quad (29)$$

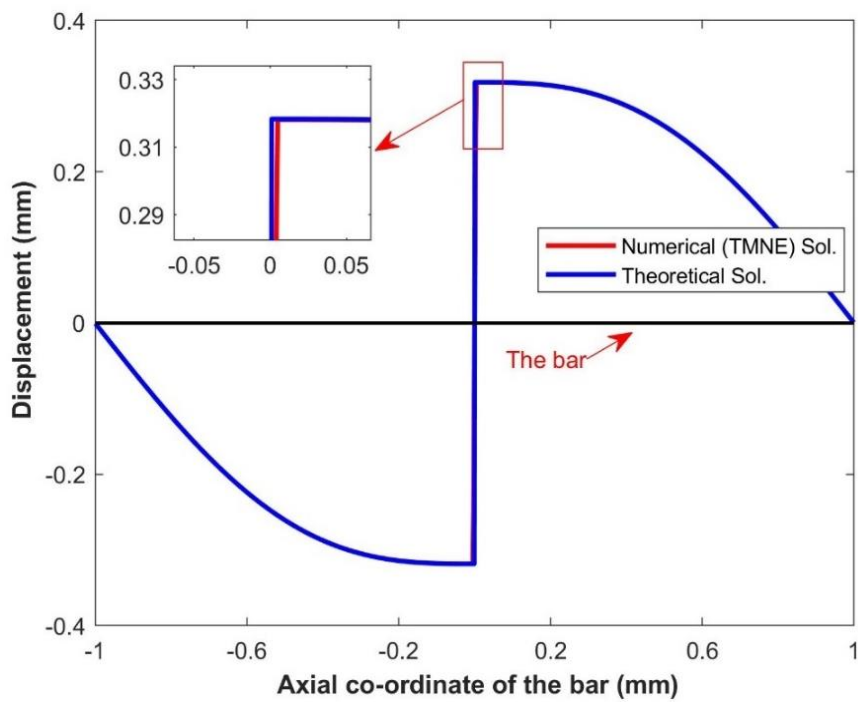
450 In order to preset the crack in the middle position, we imposed an initial history
 451 field (Borden et al., 2014) $H_0(x)$.

452
$$H_0(x) = \begin{cases} 0 & d(x) > l_0 \\ 1000 & d(x) \leq l_0 \end{cases} \quad (30)$$

453 where $d(x)$ represents the distance to the middle of the bar (i.e., $x = 0$), and L_c
 454 refers to the length-scale parameter. In this case, the analytical solution of the
 455 displacement field u_{ex} (Schillinger et al., 2015) is

456
$$u_{\text{ex}} = \begin{cases} \frac{1}{\pi^2} \sin(\pi x) - \frac{1+x}{\pi} & \text{if } x < 0 \\ \frac{1}{\pi^2} \sin(\pi x) + \frac{1-x}{\pi} & \text{if } x \geq 0 \end{cases} \quad (31)$$

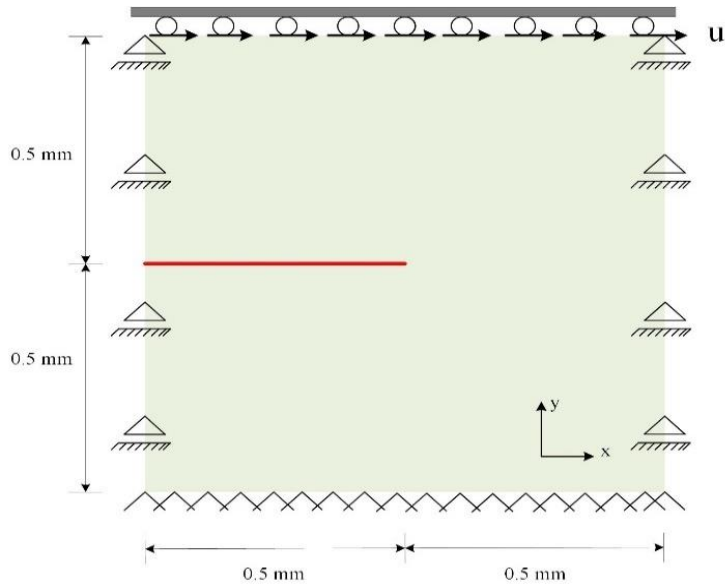
457 Fig. 10 illustrates the displacement field along the axis of the bar obtained from
 458 Eq. (31) and the proposed TMNE scheme. As shown, the displacement from our
 459 simulation is consistent with the analytical solution which demonstrates the proposed
 460 method.



461

462 Fig. 10. Displacement field along the axis of one-dimensional bar

463 4.2 Single-edge notched pure shear test



464

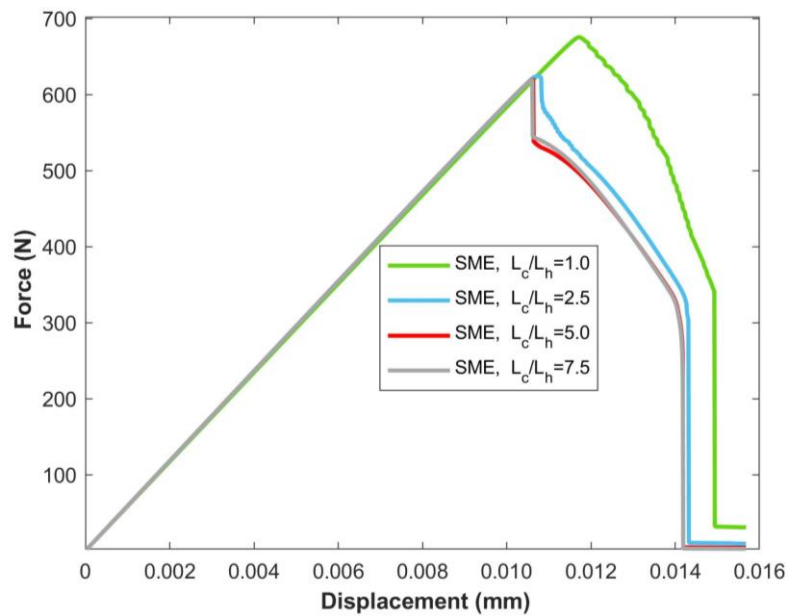
465 Fig. 11. Single edge notched model

466 The second example is a unit square plate with a horizontal notch as shown in Fig.
 467 11. This notch runs horizontally from the middle position of the left boundary to the
 468 centroid of the plate. A monotonous horizontal displacement is imposed on the upper
 469 boundary of the plate. The bottom of the plate is fully fixed while the other sides are
 470 fixed vertically. The material parameters are as follows: the elastic modulus is $E =$
 471 $2.1 \times 10^5 \text{ N/mm}^2$, Poisson's ratio is $\nu = 0.3$, the critical energy release rate is $G_c =$
 472 2.7 N/mm , and the length-scale parameter is $L_c = 0.0125 \text{ mm}$. Due to the brutal
 473 nature of the crack propagation, a displacement increment $\Delta u = 1.12 \times 10^{-5} \text{ mm}$ is
 474 used in the analysis.

475 In order to accurately resolve the high-gradient terms of ϕ , a fine mesh is required
 476 in the zone where fracture occurs. The ratio of the length-scale parameter to the element

477 size suggested by Miehe et al. (C. Miehe*,†, 2012) is $L_c / L_h = 2.0$, and for some practical
478 engineering problems, the ratio has to be $L_c / L_h = 10$ (Zhang et al., 2017b). In the phase
479 field modelling, the element size should be large to reduce the computational cost and
480 memory. In the meantime, it should be sufficiently fine to accurately capture the
481 fracture behavior. Thus, the sensitivity analysis on the element size is carried out. To
482 this end, three element sizes, namely $L_c / L_h = 1.0, 2.5$, and 5.0 (7.5) mm are selected.
483 Fig. 12a and b shows the force-displacement curves of different element sizes obtained
484 using the SME (*the traditional scheme, i.e., the Same Mesh and Element for the*
485 *damage field and displacement field*) and TMNE schemes, respectively. As can be seen,
486 the solutions of both schemes converges with decreasing element size.

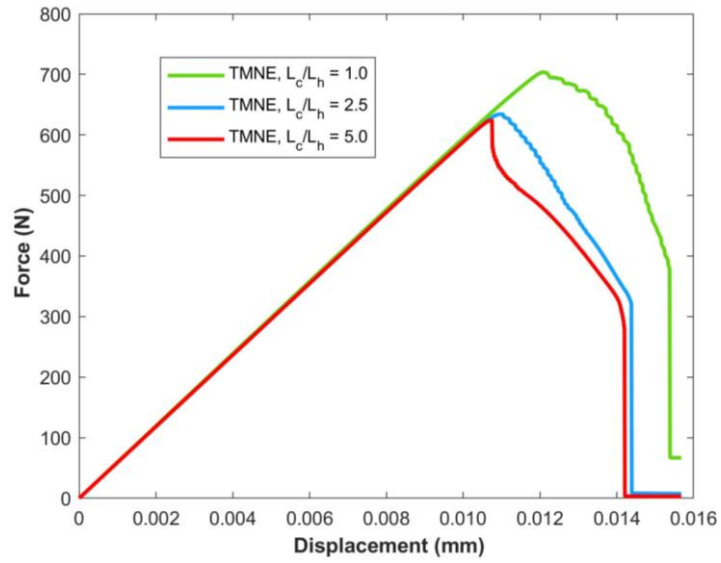
487



488

489

(a)



490

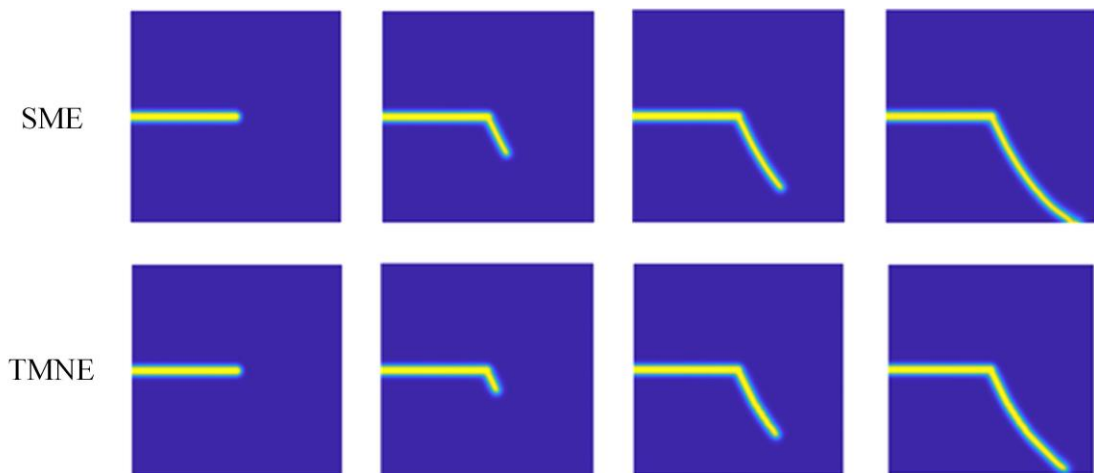
491

(b)

492 Fig. 12. Force-displacement curves of different element sizes for (a) the SME scheme

493

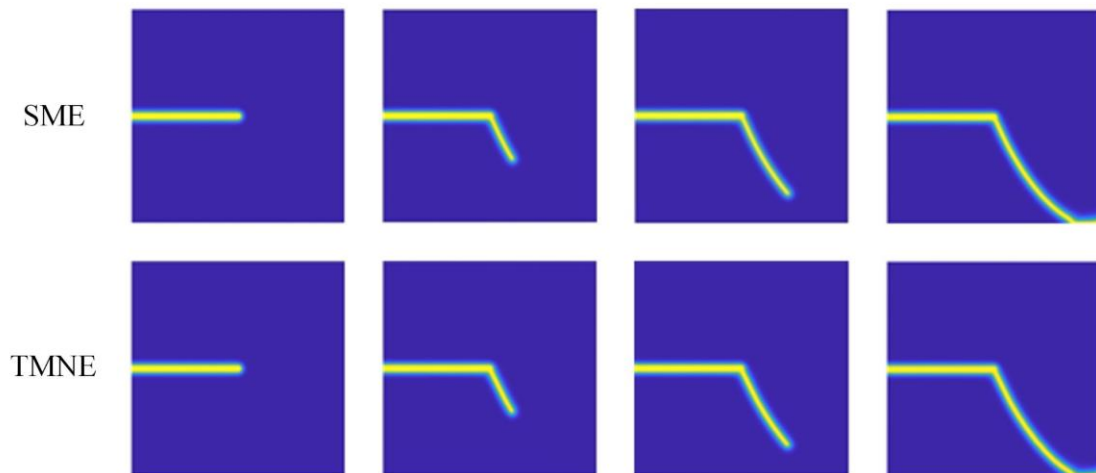
and (b) the TMNE scheme



494

495

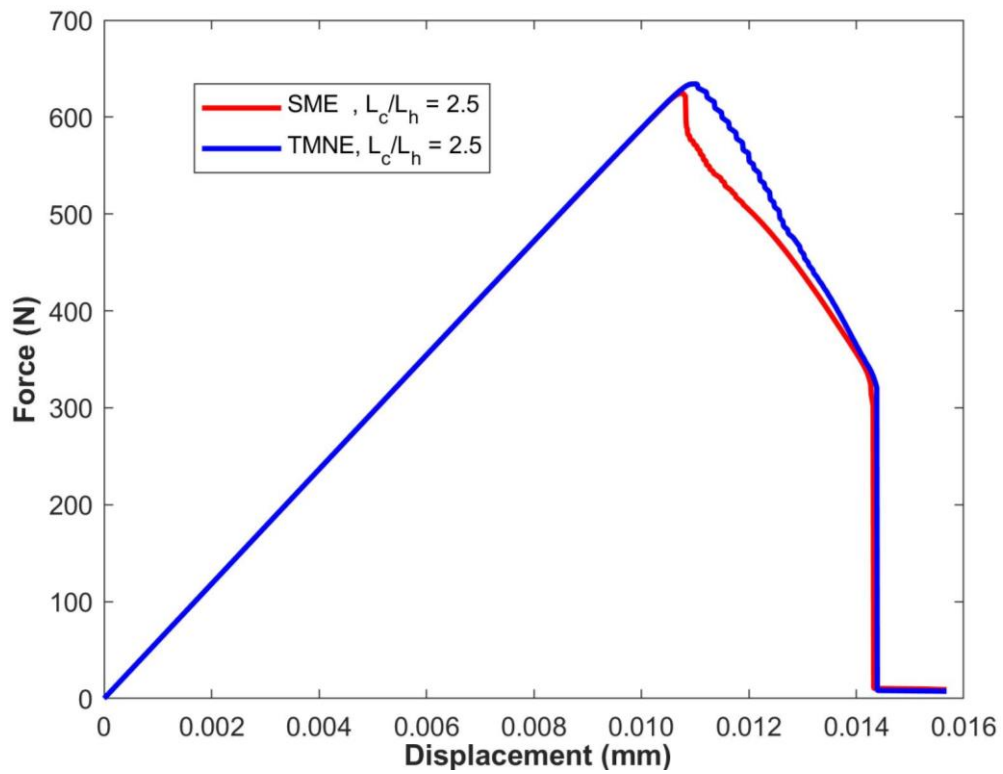
(a)



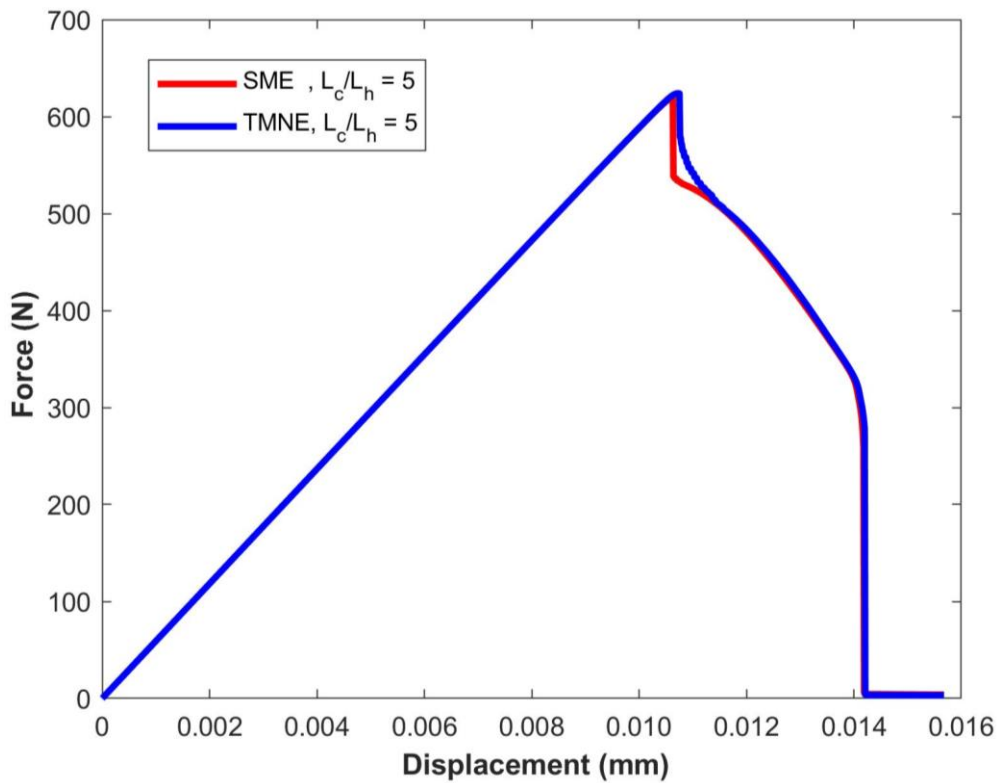
(b)

Fig. 13. Crack paths at different load stages obtained from the SME and TMNE

schemes when (a) $L_c / L_h = 2.5$ (b) $L_c / L_h = 5.0$.



(a)



504

(b)

505

506 Fig. 14. Force-displacement curves obtained using the SME and TMNE schemes, (a)

507

$$L_c / L_h = 2.5 \text{ and (b) } L_c / L_h = 5.0$$

508

509

510

511

512

513

514

For the purpose of verifying the proposed TMNE, the authors selected two element sizes, namely $L_c / L_h = 2.5$ and 5. Fig. 11 shows the crack propagation process obtained using the TMNE and SME schemes, respectively, where a good agreement is achieved in both element size cases. The force-displacement curve obtained from the TMNE is also almost consistent with that from the SME as depicted in Fig. 14, which confirms the reliability of the TMNE scheme. In terms of the computational efficiency, Table 2 provides the computational time and the number of DOFs for SME and TMNE,

515 respectively. As tabulated in Table 2 (Please see the data corresponding to the 4th order
516 model), when $L_c / L_h = 2.5$, the computational time of the TMNE scheme is 55.34% less
517 than that of the SME, and the number of DOFs is reduced by 50%; when $L_c / L_h = 5.0$,
518 the computational cost and the number of DOFs of the TMNE scheme are lower than
519 these of the SME scheme by 51.89% and 50%, respectively. The computational time
520 consumed at each time step depicted in Fig. 15 also proves this point. Moreover, the
521 force-displacement curve for $L_c / L_h = 5.0$ agree well with that for $L_c / L_h = 7.5$, as
522 depicted in Fig. 12a. Therefore, for the sake of brevity, only the element size L_c / L_h
523 =5.0 is considered below.

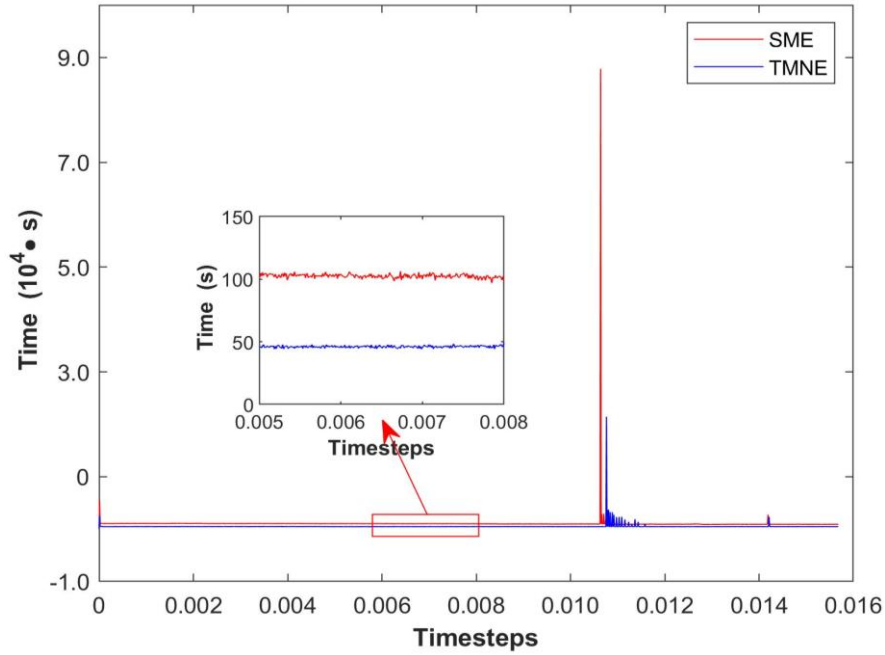
524

525 **Table 2**

526 Computational time and number of DOFs for SME and TMNE (including 2nd and 4th
527 order models)

Model	Element size	Schemes	Number of DOFs	Computing time (h)
2 nd order model	$L_c / L_h = 5.0$	SME	482403	31.3283
		TMNE	241603	19.7972
4 th order model	$L_c / L_h = 2.5$	SME	122412	9.1877
		TMNE	61206	4.1032
	$L_c / L_h = 5.0$	SME	484812	42.9266
		TMNE	242406	20.6518

528



529

530 **Fig. 15.** Computational time of SME and TMNE at each time step ($L_c / L_h = 5.0$)

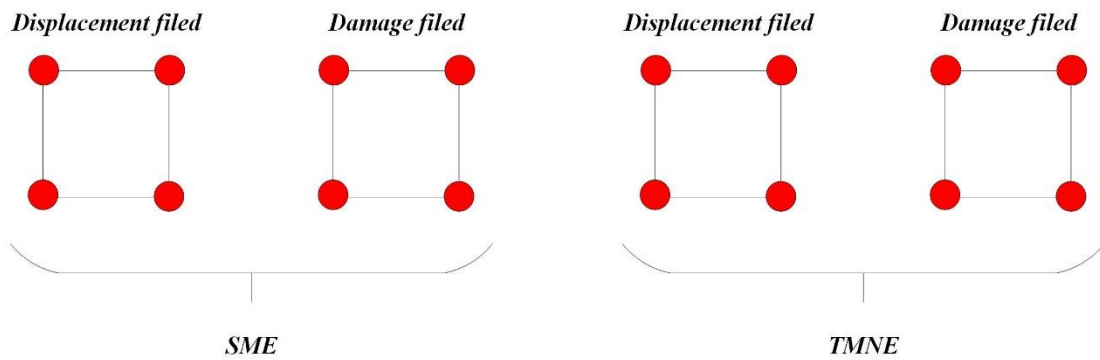
531

532 In addition, the authors also compared the performance of the TMNE against SME
 533 for the 2nd order phase field model. The element size is $L_c / L_h = 5.0$, and the other
 534 material parameters are the same as before. All the results obtained from the 2nd order
 535 model are clearly marked. Since the 2nd order model only requires C^0 continuity, both
 536 SME and TMNE schemes adopt C^0 - C^0 element combination (as depicted in Fig. 16).
 537 Fig. 17 plots the crack propagation process obtained from the two schemes, whilst Fig.
 538 18 presents the corresponding force-displacement curves. As depicted, the two
 539 simulations are basically of the same computational precision.

540 Table 2 provides the computational time for SME and TMNE. As tabulated in
 541 Table 2, in the 2nd order model, the computational time of the TMNE scheme is 36.81%

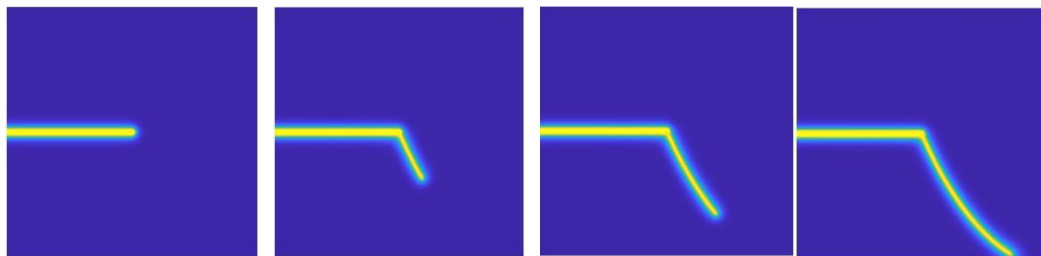
542 less than that of the SME, while in the 4th order model, it reduces the computational
 543 time by 51.89%. This is mainly because the C^1 continuity is required in the 4th order
 544 model, so compared to the equal-order elements (i.e., C^1 - C^1 combination, as depicted
 545 in Fig. 19) of SME, the TMNE scheme can adopt non-equal order elements (i.e., C^1 -
 546 C^0 combination) to further reduce computing time. In contrast, the two schemes of the
 547 2nd order model can both employ the C^0 - C^0 combination (as plotted in Fig. 16), thereby
 548 avoiding the computational cost in this regard. Moreover, the SME and TMNE schemes
 549 of the 2nd order model both require less computational time than the corresponding
 550 schemes of the 4th order model (see Table 2).

551



552

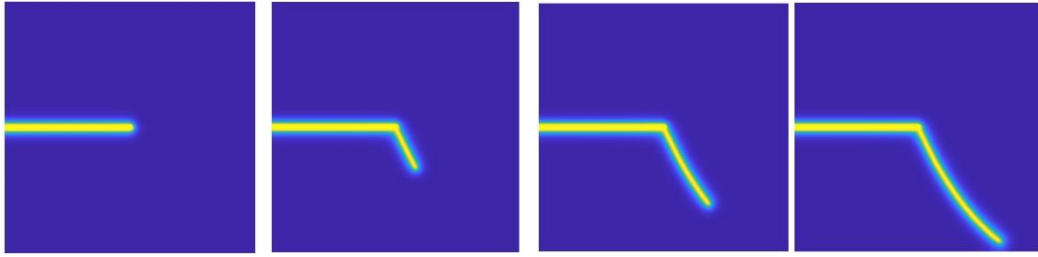
553 Fig. 16. Element types used in the SME and TMNE schemes of 2nd order model



554

555

(a)



(b)

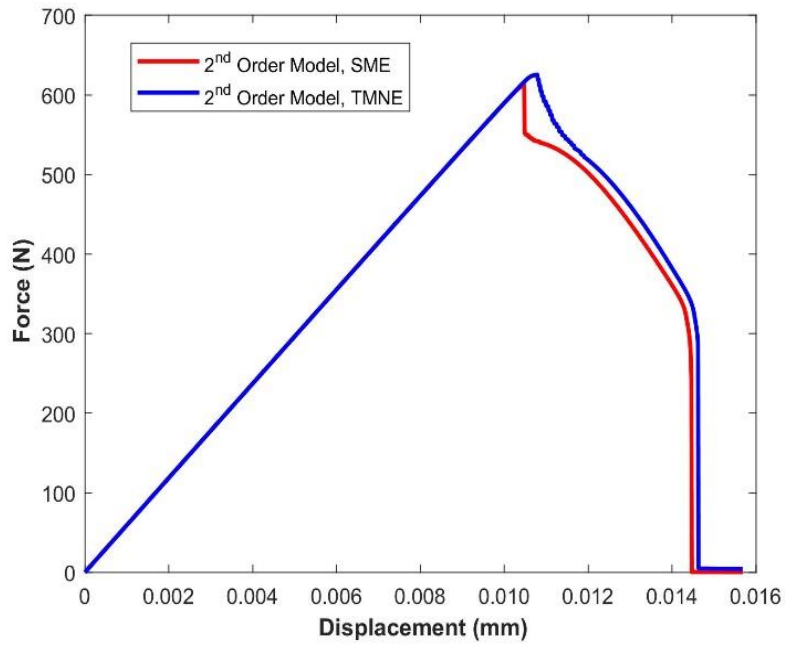
556

557

558 Fig. 17. Crack propagation of 2nd order model at different load stages for (a) the SME

559

scheme and (b) the TMNE scheme.

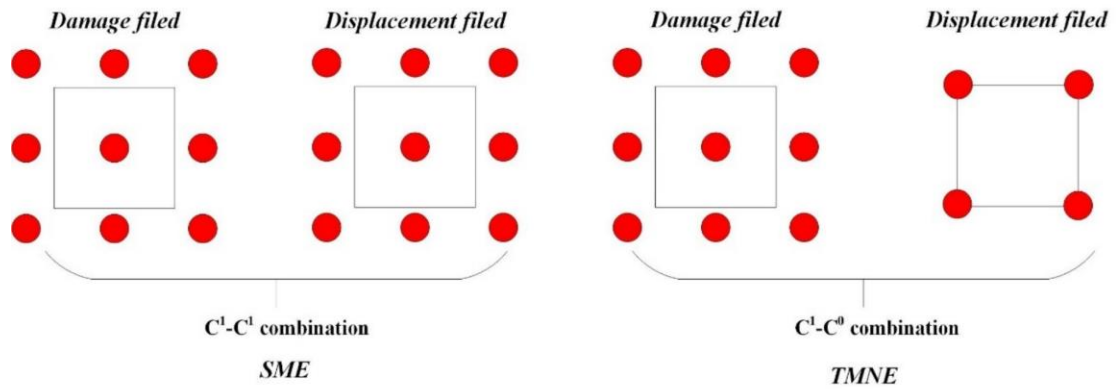


560

561 Fig. 18. Force-displacement curves obtained by SME and TMNE of 2nd order model

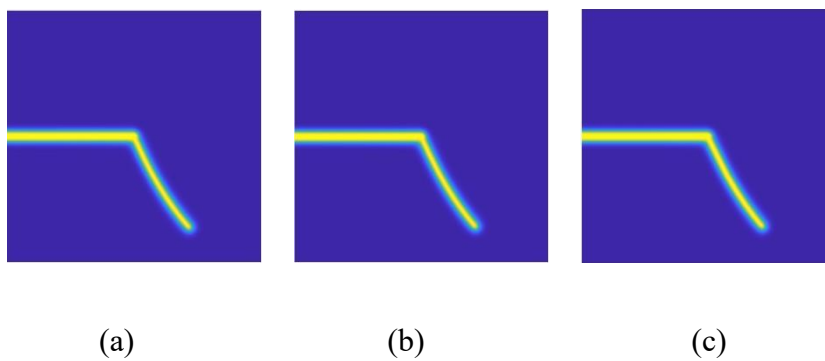
562

respectively



563

564 Fig. 19. Element types used in the SME and TMNE schemes of 4th order model



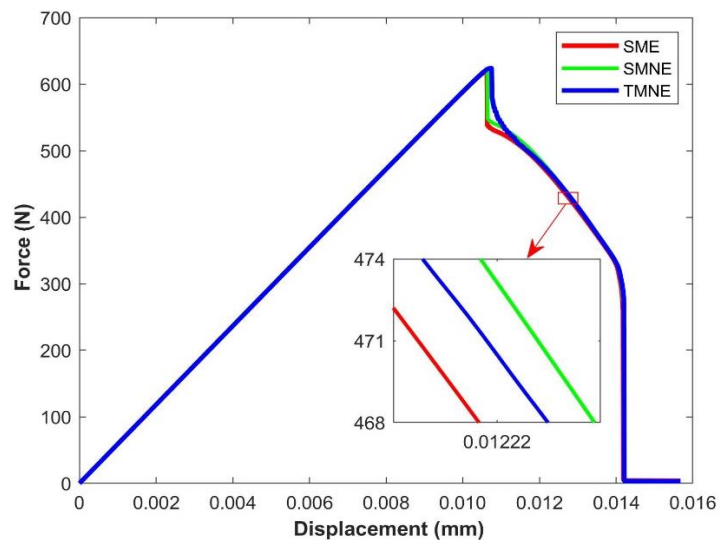
565

566

567 Fig. 20. Crack propagation at the same loading stages for (a) the SME scheme, (b) the

568

SMNE scheme, and (c) the TMNE scheme.



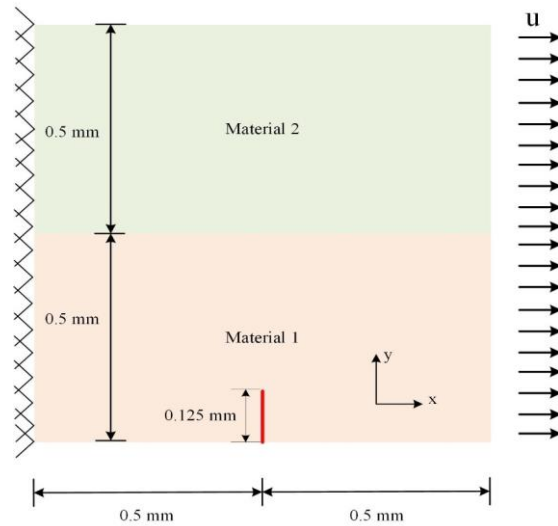
569

570 Fig. 21. Force-displacement curves obtained by SME, SMNE and TMNE respectively

571

572 Finally, the authors analyzed the influence of non-equal order elements on
573 calculation accuracy and efficiency. Fig. 20 presents the crack path from SME, SMNE
574 (i.e., the Same Mesh and Non-Equal order elements for the damage field and the
575 displacement field) and TMNE at the same loading stage, whilst Fig. 21 plots the force-
576 displacement curves. As depicted, the three simulations are of the same computational
577 precision. Notably, the TMNE simulation requires the least computational time
578 (20.6518 hours). The computational time of SMNE is 28.344h, which is 34% less than
579 that of SME. It is thus concluded that the computational time of the fourth-order phase
580 field modelling can be effectively reduced by using non-equal order elements (i.e., a C^1
581 NURBS element for the damage field and a C^0 element for the displacement field).

582 *4.3 Notched bi-material tensile test*



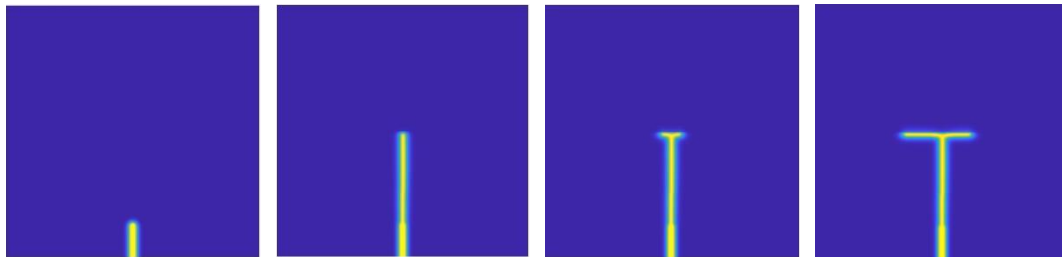
583

584

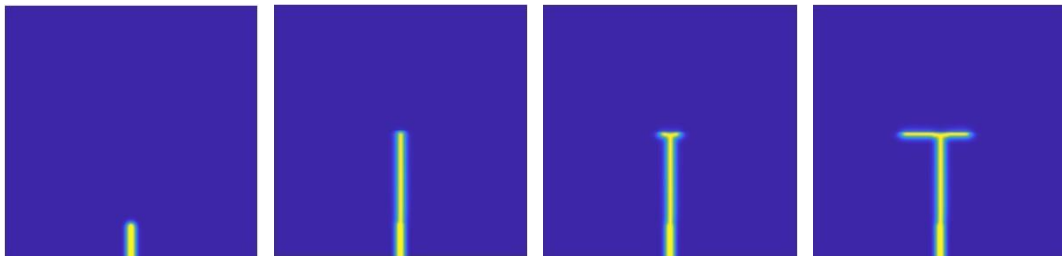
Fig. 22. Notched bi-material tensile sample

585

586 The notched tensile test is considered as the third example. The sample is made
 587 of two materials (Molnár and Gravouil, 2017) as depicted in Fig. 22. A vertical notch
 588 is located at its bottom boundary. A monotonous horizontal load is applied to the right
 589 boundary of the sample, and the left boundary is completely fixed. For material 1, the
 590 elastic modulus is $E = 3.77 \times 10^4 \text{N/mm}^2$, Poisson's ratio is $\nu = 0.2$, and the strain
 591 energy release rate is $G_c = 1.0 \text{N/mm}$; For material 2, the elastic modulus is $E =$
 592 $3.77 \times 10^5 \text{N/mm}^2$, Poisson's ratio is $\nu = 0.2$, and the strain energy release rate is
 593 $G_c = 10 \text{N/mm}$. The stiffness of material 2 and its fracture toughness are 10 times that
 594 of material 1, and their length-scale parameters are the same (i.e., $L_c = 0.01 \text{mm}$). The
 595 element size is $L_c/L_h = 5$, and the displacement increment imposed in each step is $\Delta u =$
 596 10^{-5}mm .



(a)



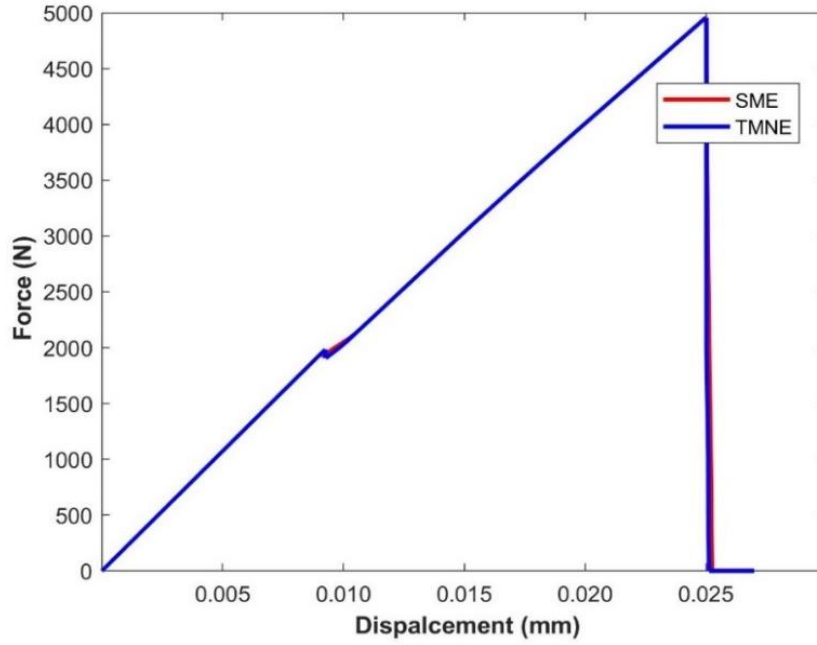
(b)

600

601 Fig. 23. Crack propagation of the notched bi-material tension sample at different
602 loading stages for (a) the SME scheme and (b) the TMNE scheme.

603

604 Fig. 23 depicts the crack propagation process obtained from the SME and TMNE
605 scheme. As plotted in Fig. 23 (a), the crack first propagates to the material transition
606 zone along the vertical direction, and then branches and propagates along the interface
607 between the two materials because cracking along the interface requires less energy
608 than piercing into the hard materials (i.e., material 2). The simulation using the TMNE
609 produces the same results as these from the SME as depicted in Fig. 23 (b). The force-
610 displacement curves from the SME and TMNE are also coincident with each other as
611 illustrated in Fig. 24 implying that the computational accuracy of TMNE is basically
612 the same as that of SME. Table 3 provides the total computational time and the number
613 of DOFs for SME and TMNE, whilst Fig. 25 plots the computational time of these two
614 schemes at each time step. As seen, the computational time of the TMNE scheme is
615 55.35% less than that of the SME, and the number of DOFs is reduced by 50.03%.



616

617 Fig. 24 Force-displacement curves of the notched bi-material tension sample

618

obtained by SME, SMNE and TMNE respectively

619

620

621

622

623

624 **Table 3**

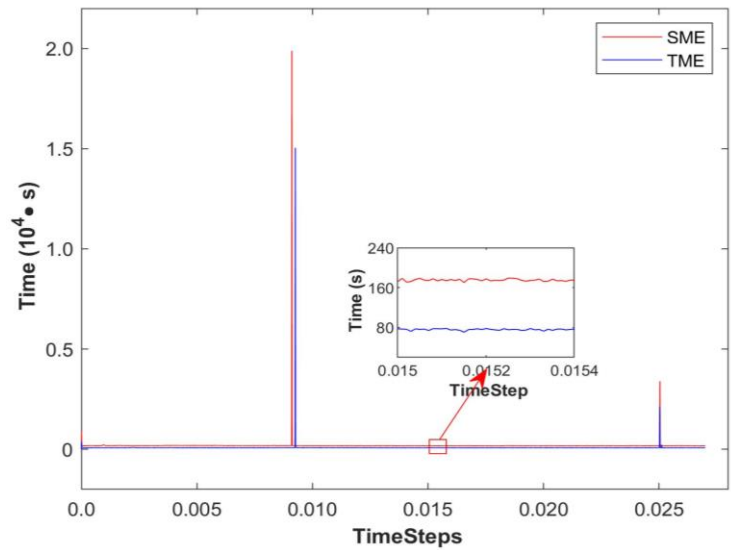
625 Computational time and number of DOFs for SME and TMNE (Notched bi-material

626 sample)

Schemes	Number of DOFs	Computational time (h)
---------	----------------	------------------------

SME	757518	147.8044
TMNE	378508	65.9918

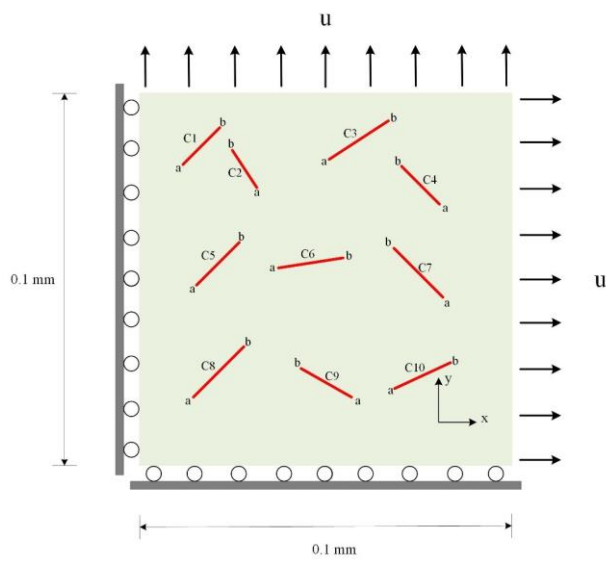
627



628

629 Fig. 25. Computational time of notched bi-material tension sample at each time step

630 *4.4 A rock-like sample with multiple cracks*



631

632 Fig. 26. A rock-like sample with multiple crack

633 **Table 4**

634 Coordinates of the pre-existing in-plate cracks

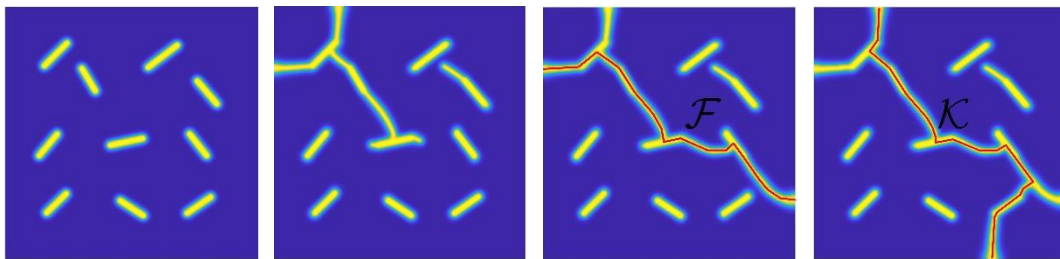
Crack ID	X _a	Y _a	X _b	Y _b
1	0.0154	0.0766	0.0244	0.0856
2	0.0357	0.0666	0.0303	0.0756
3	0.0564	0.0759	0.068	0.0847
4	0.0837	0.0615	0.0759	0.0706
5	0.0134	0.041	0.0206	0.0496
6	0.0415	0.0452	0.0544	0.0479
7	0.0796	0.041	0.0728	0.0497
8	0.0163	0.0184	0.0241	0.026
9	0.0545	0.0173	0.0454	0.0233
10	0.0718	0.0182	0.0812	0.0247

635

636 The fourth example is a rock-like sample with ten pre-existing cracks as depicted

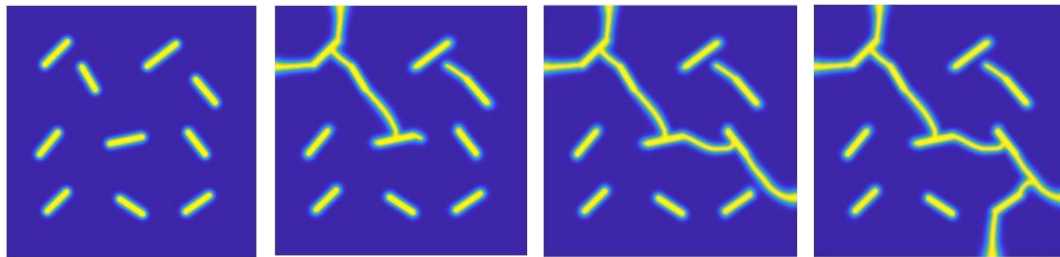
637 in Fig. 26 and Table 4. The left boundary of the sample is fixed horizontally and the

638 bottom boundary is fixed vertically. The horizontal and vertical displacements are
 639 imposed on the right and top boundaries, respectively. The elastic modulus of the
 640 sample is $E = 1 \times 10^3 \text{ N/mm}^2$, Poisson's ratio is $\nu = 0.3$, the strain energy release
 641 rate is $G_c = 1.0 \text{ N/mm}$, and the length-scale parameter is $L_c = 1 \times 10^{-3} \text{ mm}$. The
 642 element size is $L_c/L_h = 5$, and the displacement increment imposed at each step is $\Delta \mathbf{u} =$
 643 $1 \times 10^{-5} \text{ mm}$.



644

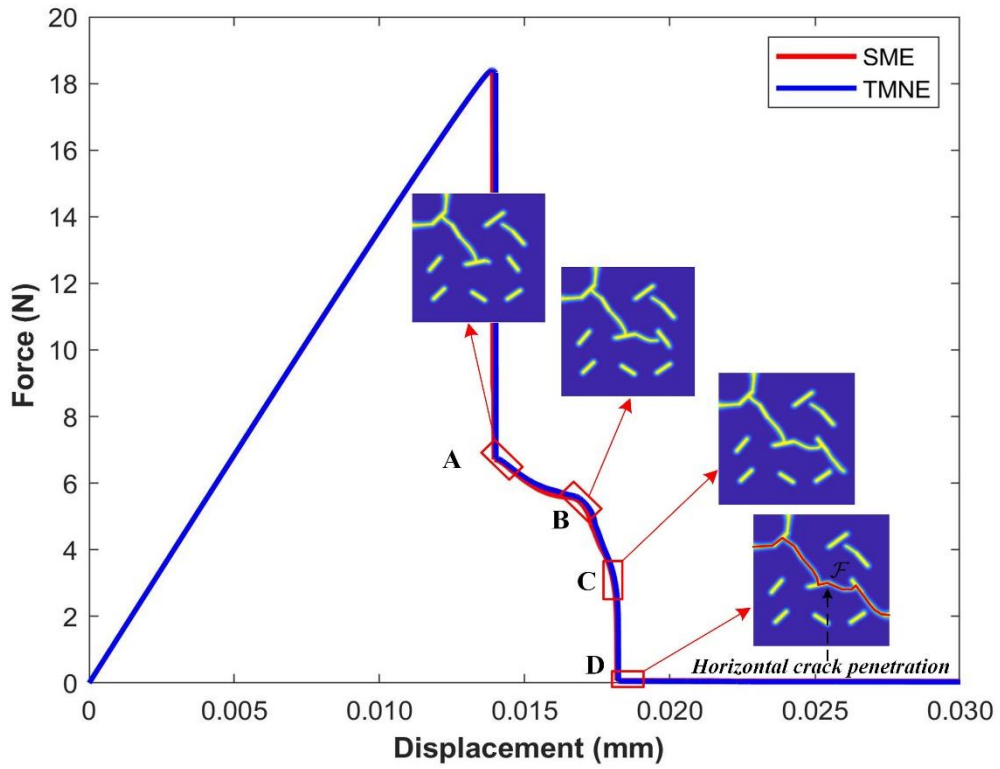
(a)



646

(b)

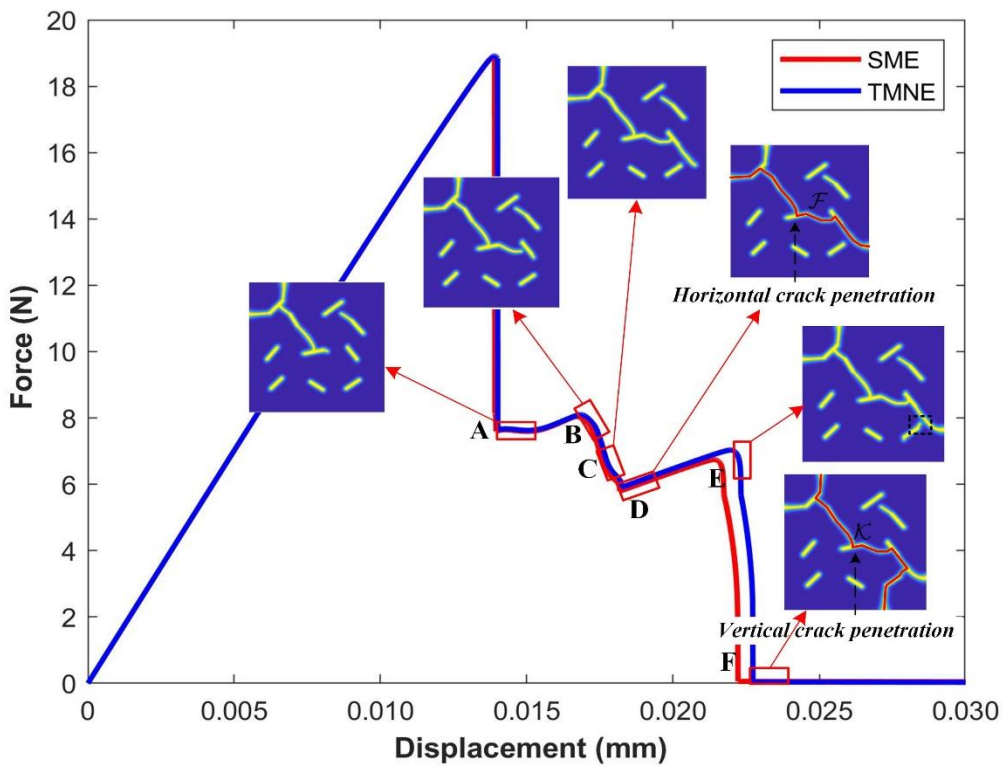
648 Fig. 27. Crack propagation of the rock-like sample with multiple cracks at different
 649 loading stages for (a) the SME scheme and (b) the TMNE scheme.



650

651 Fig. 28. Vertical force-displacement curves of the upper boundary of the rock-like

652 sample with multiple cracks obtained by SME and TMNE, respectively.



653

s

654 Fig. 29. Horizontal force-displacement curves of the right boundary of the rock-like
655 sample with multiple cracks obtained by SME and TMNE, respectively.

656 As illustrated in Fig. 27, the crack propagation process obtained from the SME
657 and the TMNE is the same. The in-plate cracks first propagate and then intersect, and
658 this process alternates until a horizontally penetrating crack \mathcal{F} and a vertical
659 penetrating crack \mathcal{K} are formed in sequence. The vertical force-displacement curve
660 obtained from the TMNE is also coincident with that from the SME as shown in Fig.
661 28, which validates the computational accuracy of the TMNE scheme. Additionally, it
662 is clearly observed that these curves have obvious turning points when a new crack or
663 a crack intersecting occurs, such as at the time points A , B , C , and D . The horizontal
664 force-displacement curves from TMNE and SME are almost in line with each other as
665 plotted in Fig. 29 except for a certain difference in the $E-F$ interval. This difference
666 is probably explained by the fact that in the $E-F$ interval, the numerical simulation is
667 in an unstable state, because the sample has already undergone penetration failure at
668 time D (i.e., crack \mathcal{F}). In terms of computational efficiency, Table 5 presents the
669 computational time and the number of DOFs for SME and TMNE, respectively, whilst
670 Fig. 30 shows the computational time of these two schemes at each time step. As
671 depicted, the computational time of the TMNE scheme is 56.09% less than that of the
672 SME, and the number of DOFs is reduced by 50%.

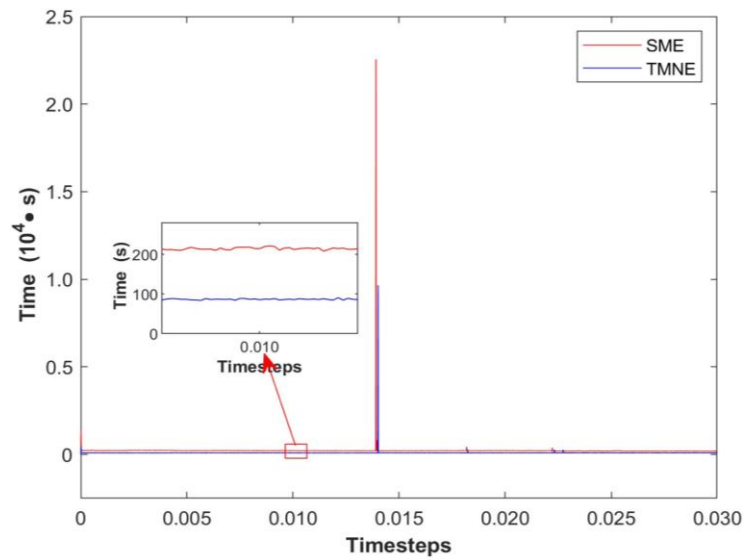
673

674

675 **Table 5**

676 Computational time and number of DOFs for SME and TMNE (the rock-like sample)

Schemes	Number of DOFs	Computational time (h)
SME	756012	185.6284
TMNE	378006	81.5102

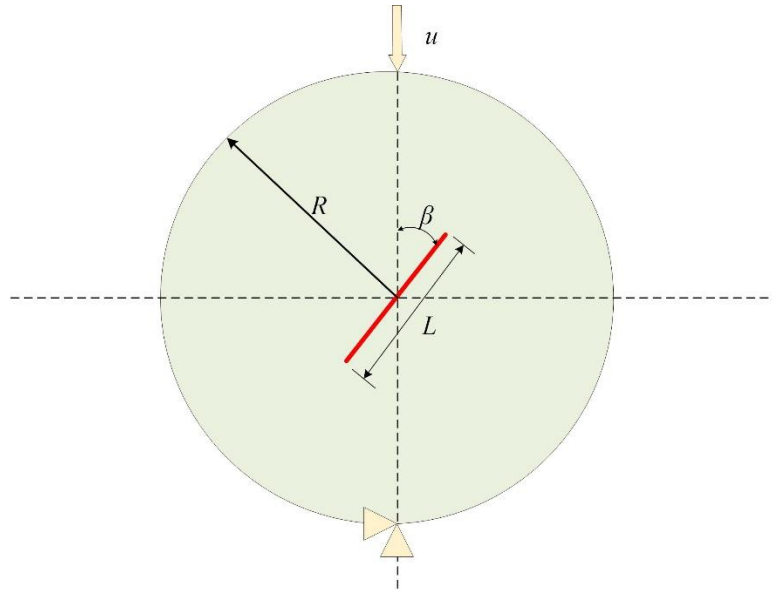


677

678 Fig. 30. Computational time of the rock-like sample with multiple cracks at each time

679 step

680 4.5 Brazilian disc sample



681

682

Fig. 31. Brazilian disc sample

683

684 Brazilian discs are widely used to measure the tensile strength of rock-like
685 materials. Therefore, this manuscript adopts the Brazilian disc to verify the applicability
686 of the TMNE scheme in rock-like materials. The sample and the boundary conditions
687 are plotted in Fig. 31, where the radius is $R = 50$ mm, the pre-existing crack length is
688 $L = 30$ mm, and the angle β takes three cases: 0° , 60° and 75° . The material
689 parameters are the same as in (Zhou et al., 2020), specifically: the elastic modulus is
690 $E = 120$ Gpa, Poisson's ratio is $\nu = 0.3$, the critical energy release rate is $G_c =$
691 30 J/m², and the length-scale parameter is $L_c = 2$ mm. Similar to the work of Zhou et
692 al. (Zhou et al., 2020), the flat end boundaries are adopted to avoid excessive stress
693 concentration. The element size is taken as $L_c/L_h = 2.0$, and a displacement increment
694 $\Delta u = 2 \times 10^{-5}$ mm is used in the analysis. In particular, the TMNE adopts equal order

695 elements (i.e., C^1 - C^1 combination) in this example to study the influence of dual meshes
696 on computing time .

697



$\beta = 0^\circ$

$\beta = 60^\circ$

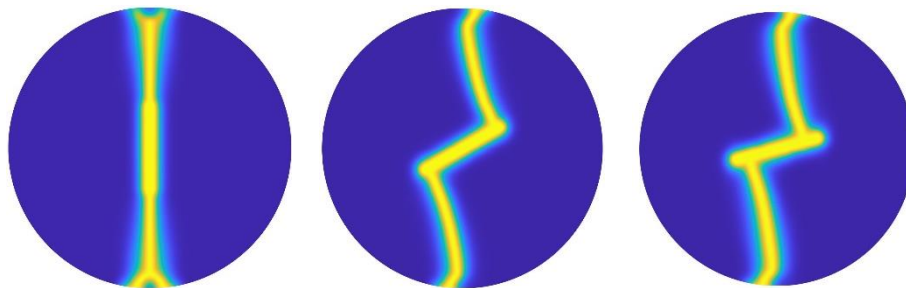
$\beta = 75^\circ$

698

699

(a)

700



$\beta = 0^\circ$

$\beta = 60^\circ$

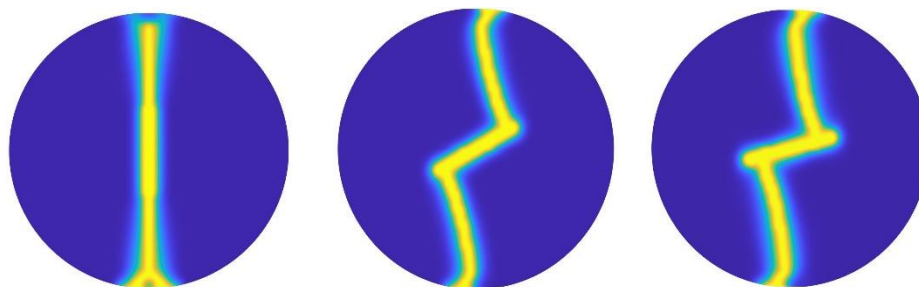
$\beta = 75^\circ$

701

702

(b)

703



$\beta = 0^\circ$

$\beta = 60^\circ$

$\beta = 75^\circ$

704

705

(c)

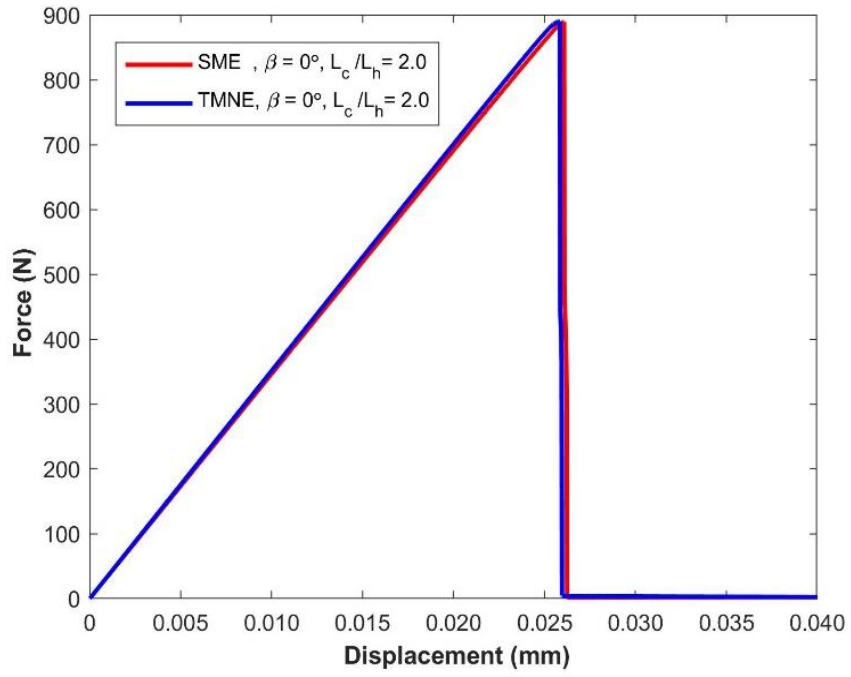
706

707 Fig. 32. Final crack path of the Brazilian disc sample obtained using (a) the
708 experiment method (Zhou et al., 2020), (b) the SME scheme, and (c) the TMNE
709 scheme.

710

711 Fig. 32 shows the final crack path obtained using the experiment method, TMNE
712 and SME at different crack inclination angles. As depicted, the crack path predicted by
713 the TMNE scheme is basically consistent with the experimental results (Zhou et al.,
714 2020) and the results of SME. The force-displacement curve obtained from the TMNE
715 is also in line with that from the SME as illustrated in Fig. 33. Therefore, the above
716 analysis indicates that the TMNE scheme is reliable and applicable to simulating the
717 crack propagation for rock-like materials. Table 6 presents the computational time and
718 the number of DOFs for SME and TMNE, respectively. As tabulated in Table 6, the
719 computing time of the dual meshes of TMNE in these three cases is 36.87%, 37.42%
720 and 38.11% less than that of the SME, respectively, and the number of DOFs is both
721 reduced by 49.47%.

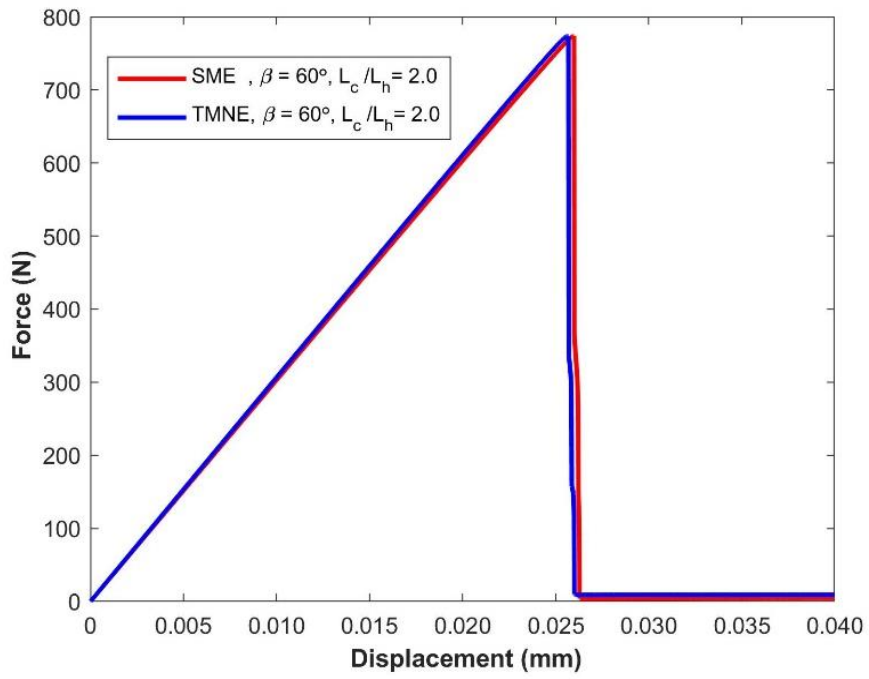
722



723

724

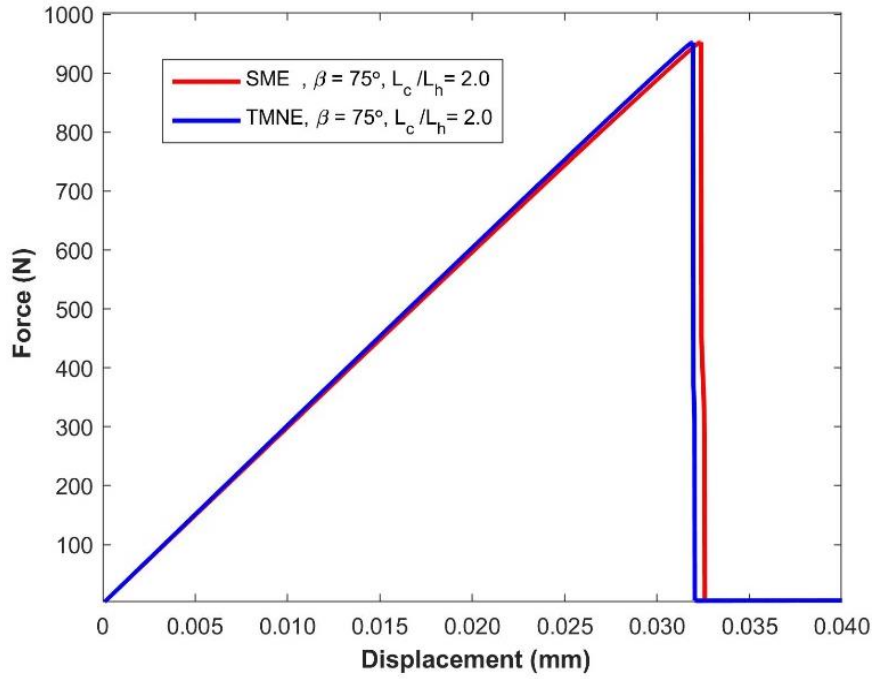
(a)



725

726

(b)



(c)

Fig. 33. Force-displacement curves of the Brazilian disc sample obtained using the SME and TMNE, (a) $\beta = 0^\circ$, (b) $\beta = 60^\circ$, and (c) $\beta = 75^\circ$.

Table 6

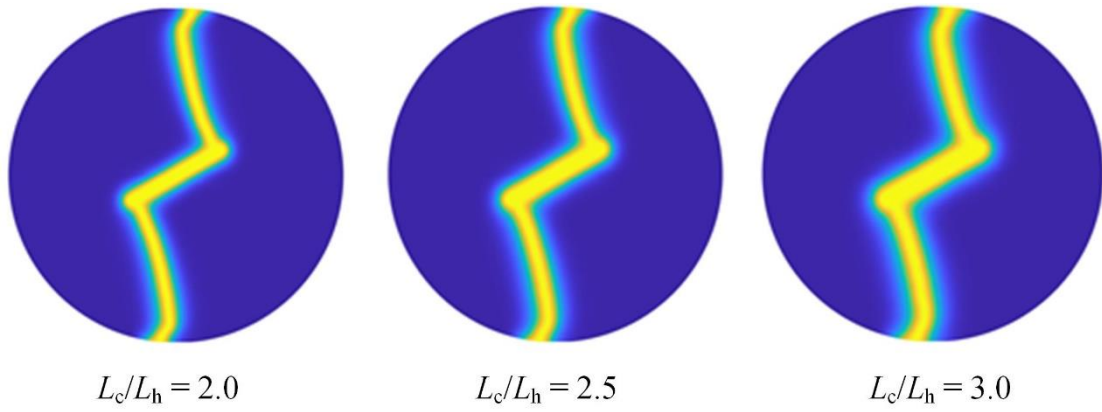
Computational time and number of DOFs for SME and TMNE (Brazilian disc sample)

Inclination angles	Schemes	Number of DOFs	Computational time (h)
$\beta = 0^\circ$	SME	75366	7.0484
	TMNE	38082	4.3621
$\beta = 60^\circ$	SME	75366	7.0272
	TMNE	38082	4.3977
$\beta = 75^\circ$	SME	75366	6.9584
	TMNE	38082	4.3928

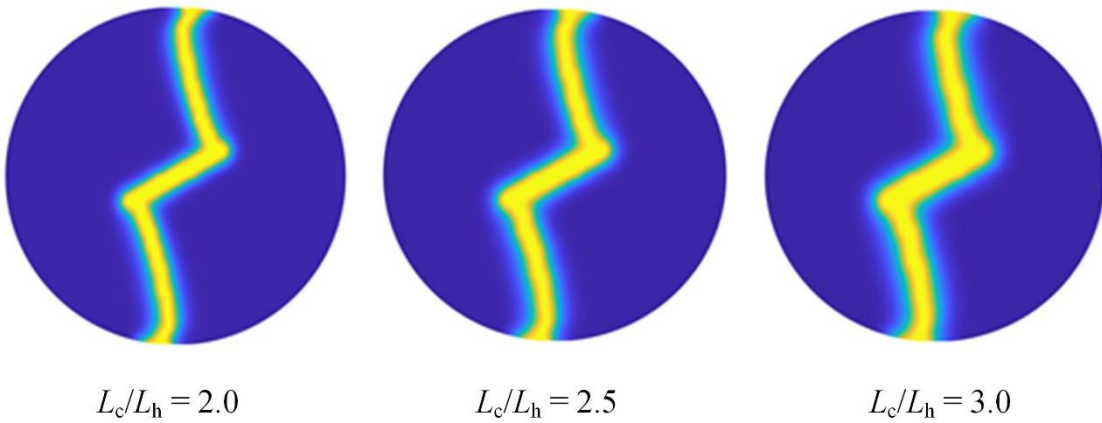
735

736 In addition, the authors also analyzed the influence of the length scale parameter
737 L_c (for fixed L_c/L_h ratio) on the results. Take the Brazilian disc with $\beta = 60^\circ$ as an
738 example. The length scale parameter L_c are respectively taken as 2.0, 2.5, 3.0 mm, and
739 the ratio of the length scale L_c to the element size L_h is fixed at 3.0. Other material
740 parameters remain unchanged.

741 Fig. 34 shows the final crack paths corresponding to different length scale
742 parameters obtained from SME and TMNE, respectively. As seen, the final crack path
743 obtained from the SME is basically consistent with that of the TMNE, and the width of
744 the crack path gradually widens as L_c increases. Fig. 35 plots the force-displacement
745 curves obtained from the SME and TMNE. As depicted, the force-displacement curves
746 obtained from the SME and TMNE both present the same trend, that is, the peak load
747 gradually decreases as L_c increases.



(a)



(b)

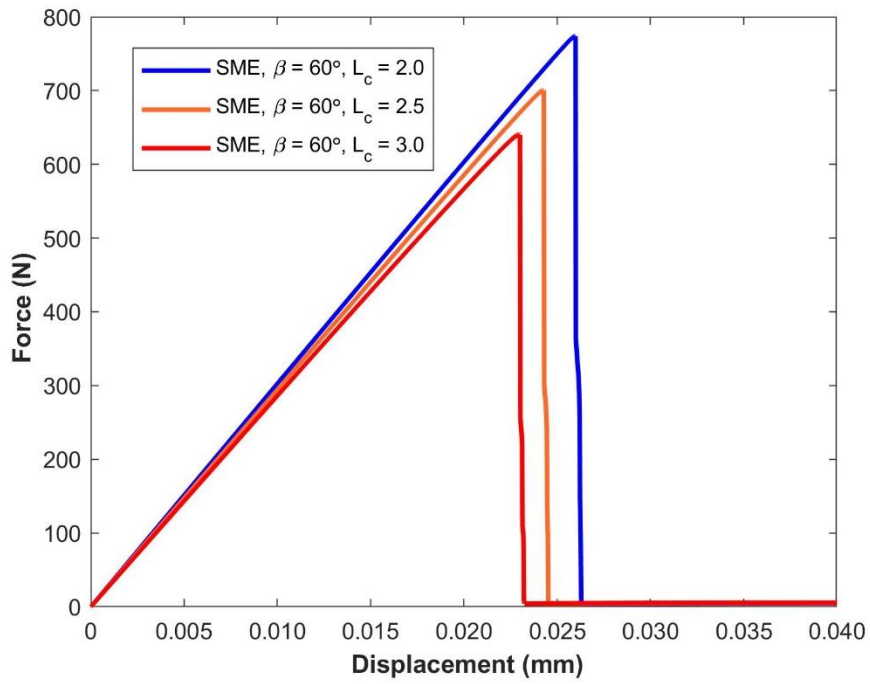
748

749 **Fig. 34.** Crack path at the final stage for (a) the SME scheme and (b) the SMNE

750

scheme

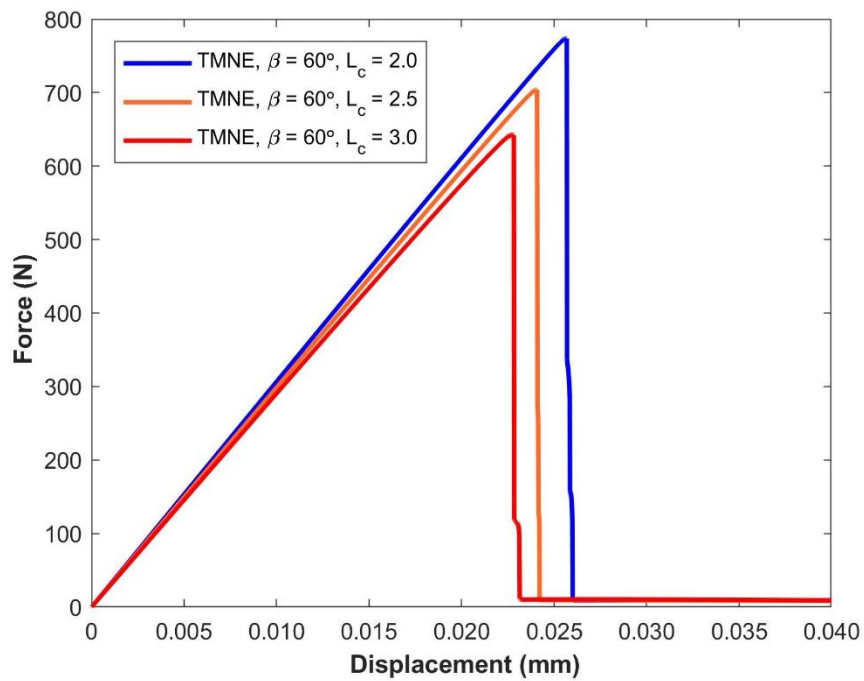
751



752

753

(a)



754

755

(b)

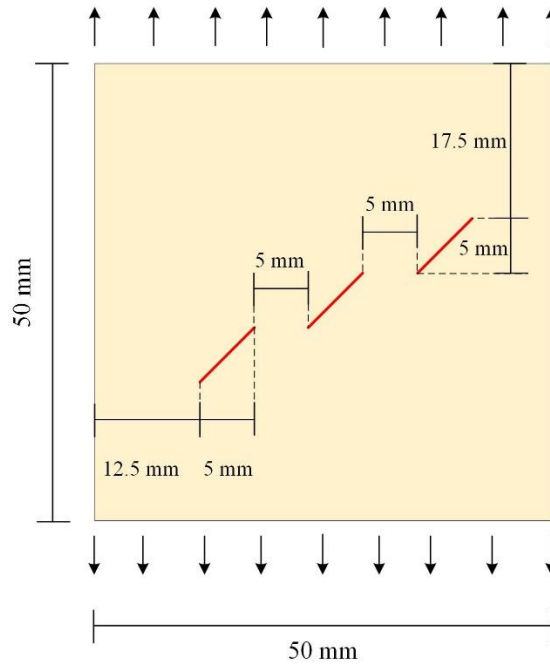
756 **Fig. 35.** Force-displacement curves of different length scale parameters, (a) the SME

757

scheme and (b) the TMNE scheme.

758

759 4.6 A square rock sample with three pre-existing cracks

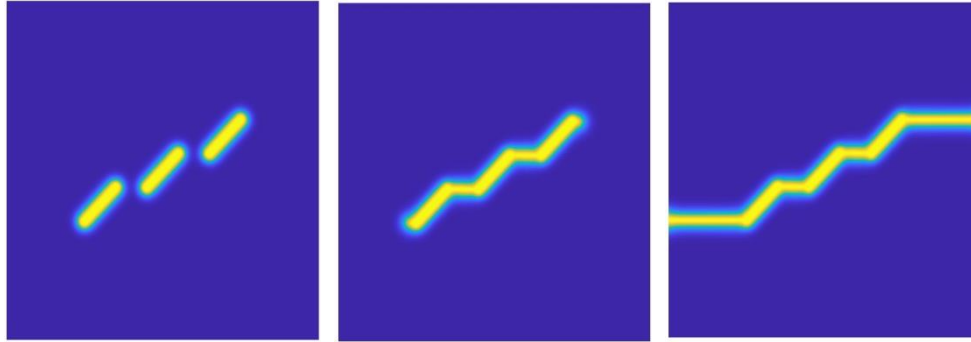


760

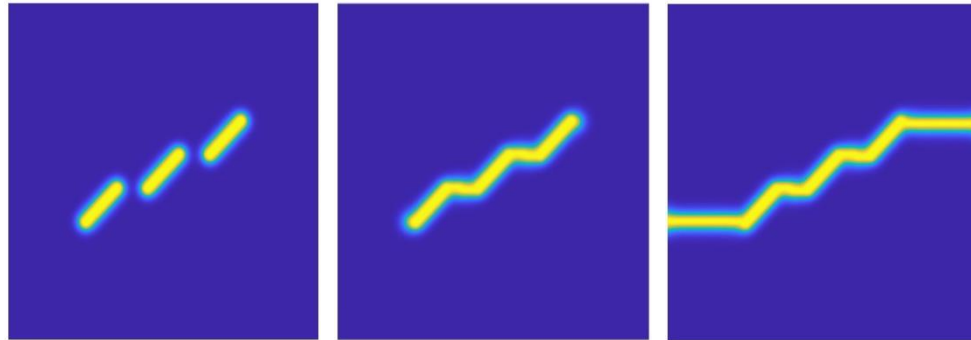
761 Fig. 36. A square rock sample with three pre-existing cracks

762

763 As depicted in Fig. 36, the square rock sample (Zhou et al., 2018) has three pre-
 764 existing cracks, and the length, spacing, and inclination angle of the three cracks are
 765 the same as each other. The length-scale parameter is $L_c = 0.75$ mm, and the other
 766 material parameters are the same as in (Zhou et al., 2018). The element size is taken as
 767 $L_c/L_h = 3.0$, and the displacement increment imposed at each step is $\Delta u =$
 768 6×10^{-6} mm.



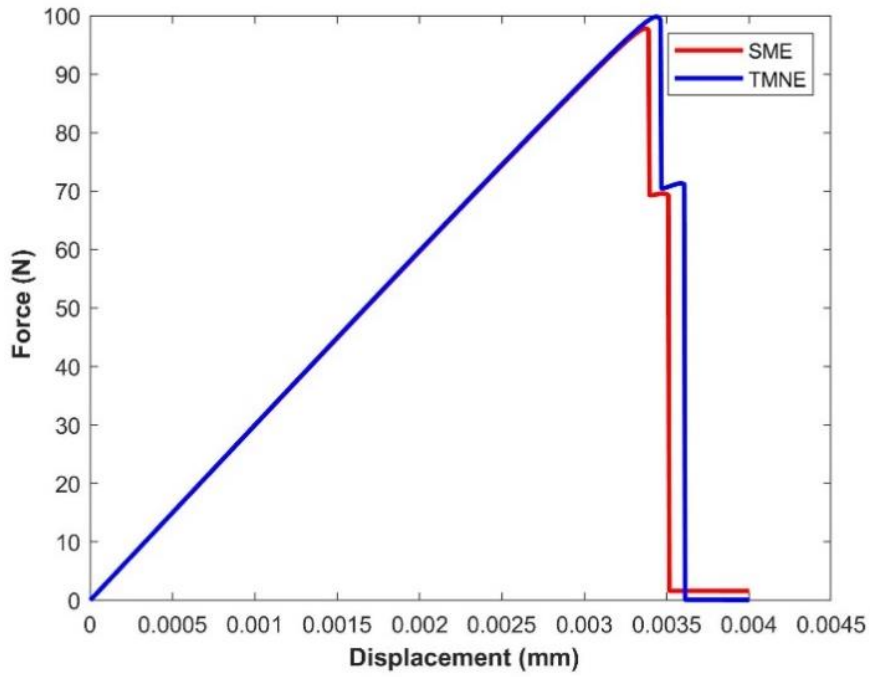
(a)



(b)

Fig. 37. Crack propagation of the square rock sample at different loading stages for (a) the SME scheme and (b) the TMNE scheme.

Fig. 37 plots the process of crack propagation obtained from the TMNE and SME where a good agreement is reached. The force-displacement curve obtained from the TMNE is also almost consistent with that from the SME as depicted in Fig.38. This further proves that the TMNE scheme is suitable for simulating the crack propagation of rock-like materials. Table 7 provides the computational time and the number of DOFs for SME and TMNE, respectively. As seen, the computational time of the TMNE is 48.51% less than that of the SME, and the number of DOFs is reduced by 50%.



783

784 Fig. 38. Force-displacement curves of the square rock sample obtained using the
 785 SME and TMNE respectively.

786 **Table 7**

787 Computational time and number of DOFs for the SME and TMNE (Square rock
 788 sample)

Schemes	Number of DOFs	Computational time (h)
SME	122412	5.1363
TMNE	61206	2.6446

789

790

791

792

793

794 **5. Conclusions**

795 High computing cost in many cases is the main barrier to the use of phase field
796 approach to study crack propagation in rock-like materials. In this manuscript, we
797 developed a novel scheme (i.e., TMNE) based on dual meshes and non-equal order
798 elements in the NURBS-based IGA framework , and then combined it with the hybrid
799 formulation of the fourth-order model to saving computing resources. The core concept
800 of the TMNE scheme is that the displacement field adopts a coarser mesh and bilinear
801 C^0 NURBS elements, whereas the damage field adopts a finer mesh and biquadratic C^1
802 NURBS elements. The number of elements used for the displacement field is 1/4 of
803 that for the damage field in 2D cases and 1/8 in 3D cases. The performance of the
804 scheme had been demonstrated by six examples with complex fracture networks,
805 including one-dimensional model, single-edge notched pure shear test, notched bi-
806 material tensile test, a rock-like sample with multiple cracks, a Brazilian disc sample,
807 and a square rock sample with three cracks. It showed that both the dual meshes and
808 the non-equal order elements can reduce the computing time by more than 30%, whilst
809 the TMNE scheme can reduce the computing time and the number of DOFS by more
810 than 50% in most cases. These results therefore indicates that there is a possibility of
811 wasting computing resources in traditional discretization of displacement field.
812 Additionally, the proposed scheme simplifies the data transfer between two meshes and
813 only one case needs to be considered, even when combined with adaptive remeshing,
814 because the correspondence between two meshes is fixed.

815 Notably, the proposed scheme can also be extended to a variety of NURBS
816 elements (C^0 - C^4) as required. Future work will include adaptive remeshing and multi-
817 field crack propagation under TMNE framework.

818 **6 Acknowledgement**

819 The authors are pleased to acknowledge the support from the National Natural
820 Science Foundation of China (Projects 51890912, 51979025 and 52011530189) and the
821 Open Research Fund of State Key Laboratory of Coastal and Offshore Engineering,
822 Dalian University of Technology (Project LP1926).

823

824

825

826

827

828

829

830

831 **Reference**

- 832 Ambati, M., Gerasimov, T., De Lorenzis, L., 2015. Phase-field modeling of ductile
833 fracture. *Comput. Mech.* 55, 1017–1040. [https://doi.org/10.1007/s00466-015-](https://doi.org/10.1007/s00466-015-1151-4)
834 1151-4
- 835 Ambati, M., Gerasimov, T., De Lorenzis, L., 2014. A review on phase-field models of
836 brittle fracture and a new fast hybrid formulation. *Comput. Mech.* 55, 383–405.
837 <https://doi.org/10.1007/s00466-014-1109-y>
- 838 Ambati, M., Kruse, R., De Lorenzis, L., 2016. A phase-field model for ductile
839 fracture at finite strains and its experimental verification. *Comput. Mech.* 57,
840 149–167. <https://doi.org/10.1007/s00466-015-1225-3>
- 841 Amiri, F., Millán, D., Shen, Y., Rabczuk, T., Arroyo, M., 2014. Phase-field modeling
842 of fracture in linear thin shells. *Theor. Appl. Fract. Mech.* 69, 102–109.
843 <https://doi.org/10.1016/j.tafmec.2013.12.002>
- 844 Bauchy, M., Laubie, H., Abdolhosseini Qomi, M.J., Hoover, C.G., Ulm, F.J., Pellenq,
845 R.J.M., 2015. Fracture toughness of calcium-silicate-hydrate from molecular
846 dynamics simulations. *J. Non. Cryst. Solids* 419.
847 <https://doi.org/10.1016/j.jnoncrysol.2015.03.031>
- 848 Biben, T., Kassner, K., Misbah, C., 2005. Phase-field approach to three-dimensional
849 vesicle dynamics. *Phys. Rev. E - Stat. Nonlinear, Soft Matter Phys.* 72, 1–15.
850 <https://doi.org/10.1103/PhysRevE.72.041921>

851 Boettinger, W.J., Warren, J.A., Beckermann, C., Karma, A., 2002. Phase-field
852 simulation of solidification. *Annu. Rev. Mater. Sci.* 32, 163–194.
853 <https://doi.org/10.1146/annurev.matsci.32.101901.155803>

854 Borden, M., 2012. Isogeometric analysis of phase-field models for dynamic brittle
855 and ductile fracture. Thesis.

856 Borden, M.J., Hughes, T.J.R., Landis, C.M., Anvari, A., Lee, I.J., 2016. A phase-field
857 formulation for fracture in ductile materials: Finite deformation balance law
858 derivation, plastic degradation, and stress triaxiality effects. *Comput. Methods*
859 *Appl. Mech. Eng.* 312, 130–166. <https://doi.org/10.1016/j.cma.2016.09.005>

860 Borden, M.J., Hughes, T.J.R., Landis, C.M., Verhoosel, C. V., 2014. A higher-order
861 phase-field model for brittle fracture: Formulation and analysis within the
862 isogeometric analysis framework. *Comput. Methods Appl. Mech. Eng.* 273,
863 100–118. <https://doi.org/10.1016/j.cma.2014.01.016>

864 Borden, M.J., Verhoosel, C. V., Scott, M.A., Hughes, T.J.R., Landis, C.M., 2012. A
865 phase-field description of dynamic brittle fracture. *Comput. Methods Appl.*
866 *Mech. Eng.* 217–220, 77–95. <https://doi.org/10.1016/j.cma.2012.01.008>

867 Bourdin, B., Francfort, G.A., Marigo, J.J., 2000. Numerical experiments in revisited
868 brittle fracture. *J. Mech. Phys. Solids* 48, 797–826.
869 [https://doi.org/10.1016/S0022-5096\(99\)00028-9](https://doi.org/10.1016/S0022-5096(99)00028-9)

870 C. Miehe*,†, F.W. and M.H.I., 2012. Thermodynamically consistent phase-field
871 models of fracture: Variational principles and multi-field FE implementations.
872 International 1102–1119. <https://doi.org/10.1002/nme>

873 Chen, J.-S., Hillman, M., Chi, S.-W., 2017. Meshfree Methods: Progress Made after
874 20 Years. *J. Eng. Mech.* 143, 04017001. [https://doi.org/10.1061/\(asce\)em.1943-](https://doi.org/10.1061/(asce)em.1943-)
875 7889.0001176

876 Chen, L., Li, B., de Borst, R., 2020. Adaptive isogeometric analysis for phase-field
877 modeling of anisotropic brittle fracture. *Int. J. Numer. Methods Eng.* 121, 4630–
878 4648. <https://doi.org/10.1002/nme.6457>

879 Deng, J., Chen, F., Li, X., Hu, C., Tong, W., Yang, Z., Feng, Y., 2008. Polynomial
880 splines over hierarchical T-meshes. *Graph. Models* 70, 76–86.
881 <https://doi.org/10.1016/j.gmod.2008.03.001>

882 Ebrahim, F., Bamer, F., Markert, B., 2018. The influence of the network topology on
883 the deformation and fracture behaviour of silica glass: A molecular dynamics
884 study. *Comput. Mater. Sci.* 149.
885 <https://doi.org/10.1016/j.commatsci.2018.03.017>

886 Fei, F., Choo, J., 2020. A phase-field model of frictional shear fracture in geologic
887 materials. *Comput. Methods Appl. Mech. Eng.* 369, 113265.
888 <https://doi.org/10.1016/j.cma.2020.113265>

889 Francfort, G.A., Marigo, J.J., 1998. Revisiting brittle fracture as an energy
890 minimization problem. *J. Mech. Phys. Solids* 46, 1319–1342.
891 [https://doi.org/10.1016/S0022-5096\(98\)00034-9](https://doi.org/10.1016/S0022-5096(98)00034-9)

892 Franklin, W.S., 1916. Statistical physics. *Science* (80-.).
893 <https://doi.org/10.1126/science.44.1127.158>

894 Gao, Y., Li, B., Wang, J., Feng, X.Q., 2021. Fracture toughness analysis of helical
895 fiber-reinforced biocomposites. *J. Mech. Phys. Solids* 146.
896 <https://doi.org/10.1016/j.jmps.2020.104206>

897 Gao, Y., Liu, Z., Wang, T., Zeng, Q., Li, X., Zhuang, Z., 2019. XFEM modeling for
898 curved fracture in the anisotropic fracture toughness medium. *Comput. Mech.*
899 63, 869–883. <https://doi.org/10.1007/s00466-018-1627-0>

900 Garau, E.M., Vázquez, R., 2018. Algorithms for the implementation of adaptive
901 isogeometric methods using hierarchical B-splines. *Appl. Numer. Math.* 123, 58–
902 87. <https://doi.org/10.1016/j.apnum.2017.08.006>

903 Geelen, R.J.M., Liu, Y., Hu, T., Tupek, M.R., Dolbow, J.E., 2019. A phase-field
904 formulation for dynamic cohesive fracture. *Comput. Methods Appl. Mech. Eng.*
905 348, 680–711. <https://doi.org/10.1016/j.cma.2019.01.026>

906 Ghandriz, R., Hart, K., Li, J., 2020. Extended finite element method (XFEM)
907 modeling of fracture in additively manufactured polymers. *Addit. Manuf.* 31.
908 <https://doi.org/10.1016/j.addma.2019.100945>

909 Goswami, S., 2020. Phase field modeling of fracture with isogeometric analysis and
910 machine learning methods.

911 Goswami, S., Anitescu, C., Chakraborty, S., Rabczuk, T., 2020a. Transfer learning
912 enhanced physics informed neural network for phase-field modeling of fracture.
913 Theor. Appl. Fract. Mech. 106, 102447.
914 <https://doi.org/10.1016/j.tafmec.2019.102447>

915 Goswami, S., Anitescu, C., Rabczuk, T., 2020b. Adaptive fourth-order phase field
916 analysis for brittle fracture. Comput. Methods Appl. Mech. Eng. 361, 112808.
917 <https://doi.org/10.1016/j.cma.2019.112808>

918 Goswami, S., Anitescu, C., Rabczuk, T., 2020c. Adaptive fourth-order phase field
919 analysis using deep energy minimization. Theor. Appl. Fract. Mech. 107,
920 102527. <https://doi.org/10.1016/j.tafmec.2020.102527>

921 Goswami, S., Anitescu, C., Rabczuk, T., 2019. Adaptive phase field analysis with
922 dual hierarchical meshes for brittle fracture. Eng. Fract. Mech. 218, 106608.
923 <https://doi.org/10.1016/j.engfracmech.2019.106608>

924 Goswami, S., Yin, M., Yu, Y., Karniadakis, G., 2021a. A physics-informed
925 variational DeepONet for predicting the crack path in brittle materials.

926 Goswami, S., Yin, M., Yu, Y., Karniadakis, G., 2021b. A physics-informed
927 variational DeepONet for predicting the crack path in brittle materials.

928 Hirshikesh, H., Pramod, A.L.N., Waisman, H., Natarajan, S., 2021. Adaptive phase
929 field method using novel physics based refinement criteria. *Comput. Methods*
930 *Appl. Mech. Eng.* 383, 113874. <https://doi.org/10.1016/j.cma.2021.113874>

931 Hirshikesh, Pramod, A.L.N., Annabattula, R.K., Ooi, E.T., Song, C., Natarajan, S.,
932 2019. Adaptive phase-field modeling of brittle fracture using the scaled
933 boundary finite element method. *Comput. Methods Appl. Mech. Eng.* 355, 284–
934 307. <https://doi.org/10.1016/j.cma.2019.06.002>

935 Hu, X., Li, R., Tang, T., 2009. A multi-mesh adaptive finite element approximation to
936 phase field models. *Commun. Comput. Phys.* 5, 1012–1029.

937 Huang, C., Gao, X., 2020. Phase field modeling of hydrogen embrittlement. *Int. J.*
938 *Hydrogen Energy* 45, 20053–20068.
939 <https://doi.org/10.1016/j.ijhydene.2020.05.015>

940 Huang, C., Gao, X., 2019. Development of a phase field method for modeling brittle
941 and ductile fracture. *Comput. Mater. Sci.* 169, 109089.
942 <https://doi.org/10.1016/j.commatsci.2019.109089>

943 Hughes, T.J.R., Cottrell, J.A., Bazilevs, Y., 2005. Isogeometric analysis: CAD, finite
944 elements, NURBS, exact geometry and mesh refinement. *Comput. Methods*
945 *Appl. Mech. Eng.* 194, 4135–4195. <https://doi.org/10.1016/j.cma.2004.10.008>

946 Li, X., Deng, J., Chen, F., 2010. Polynomial splines over general T-meshes. *Vis.*
947 *Comput.* 26, 277–286. <https://doi.org/10.1007/s00371-009-0410-9>

948 Meng, Q., Li, B., Li, T., Feng, X.Q., 2018. Effects of nanofiber orientations on the
949 fracture toughness of cellulose nanopaper. *Eng. Fract. Mech.* 194, 350–361.
950 <https://doi.org/10.1016/j.engfracmech.2018.03.034>

951 Menon, S., Song, X., 2021a. A stabilized computational nonlocal poromechanics
952 model for dynamic analysis of saturated porous media. *Int. J. Numer. Methods*
953 *Eng.* 122, 5512–5539. <https://doi.org/10.1002/nme.6762>

954 Menon, S., Song, X., 2021b. A computational periporomechanics model for localized
955 failure in unsaturated porous media. *Comput. Methods Appl. Mech. Eng.* 384,
956 113932. <https://doi.org/10.1016/j.cma.2021.113932>

957 Menon, S., Song, X., 2019. Coupled analysis of desiccation cracking in unsaturated
958 soils through a non-local mathematical formulation. *Geosci.* 9.
959 <https://doi.org/10.3390/geosciences9100428>

960 Menon, S., Song, X., n.d. Computational multiphase periporomechanics for unguided
961 cracking in unsaturated porous media 1–36.

962 Miehe, C., Hofacker, M., Welschinger, F., 2010. A phase field model for rate-
963 independent crack propagation: Robust algorithmic implementation based on
964 operator splits. *Comput. Methods Appl. Mech. Eng.* 199, 2765–2778.
965 <https://doi.org/10.1016/j.cma.2010.04.011>

966 Miehe, C., Schänzel, L.M., 2014. Phase field modeling of fracture in rubbery
967 polymers. Part I: Finite elasticity coupled with brittle failure. *J. Mech. Phys.*
968 *Solids* 65, 93–113. <https://doi.org/10.1016/j.jmps.2013.06.007>

969 Molnár, G., Gravouil, A., 2017. (Bi-material model)2D and 3D Abaqus
970 implementation of a robust staggered phase-field solution for modeling brittle
971 fracture. *Finite Elem. Anal. Des.* 130, 27–38.
972 <https://doi.org/10.1016/j.finel.2017.03.002>

973 Muixí, A., Fernández-Méndez, S., Rodríguez-Ferran, A., 2020. Adaptive refinement
974 for phase-field models of brittle fracture based on Nitsche’s method. *Comput.*
975 *Mech.* 66, 69–85. <https://doi.org/10.1007/s00466-020-01841-1>

976 Nguyen, K.D., E.Augarde, C., Coombs, W.M., Nguyen-Xuan, H., Abdel-Wahab, M.,
977 2020. Non-conforming multipatches for NURBS-based finite element analysis of
978 higher-order phase-field models for brittle fracture. *Eng. Fract. Mech.* 235,
979 107133. <https://doi.org/10.1016/j.engfracmech.2020.107133>

980 Nguyen, S., Folch, R., Verma, V.K., Henry, H., Plapp, M., 2010. Phase-field
981 simulations of viscous fingering in shear-thinning fluids. *Phys. Fluids* 22.
982 <https://doi.org/10.1063/1.3494550>

983 Ni, L., Zhang, X., Zou, L., Huang, J., 2020. Phase-field modeling of hydraulic
984 fracture network propagation in poroelastic rocks. *Comput. Geosci.* 24, 1767–
985 1782. <https://doi.org/10.1007/s10596-020-09955-4>

986 Orozco, L.F., Delenne, J.Y., Sornay, P., Radjai, F., 2019. Discrete-element model for
987 dynamic fracture of a single particle. *Int. J. Solids Struct.* 166, 47–56.
988 <https://doi.org/10.1016/j.ijsolstr.2019.01.033>

989 Paul, K., Zimmermann, C., Mandadapu, K.K., Hughes, T.J.R., Landis, C.M., Sauer,
990 R.A., 2020. An adaptive space-time phase field formulation for dynamic fracture
991 of brittle shells based on LR NURBS. *Comput. Mech.* 65, 1039–1062.
992 <https://doi.org/10.1007/s00466-019-01807-y>

993 Piegl, L., Tiller, W., 1997. *The NURBS book*, 2nd edition. Springer-Verlag.

994 Rabczuk, T., 2013. *Computational Methods for Fracture in Brittle and Quasi-Brittle*
995 *Solids: State-of-the-Art Review and Future Perspectives*. *ISRN Appl. Math.*
996 2013, 1–38. <https://doi.org/10.1155/2013/849231>

997 Remacle, J., Lambrechts, J., Seny, B., 2012. A phase-field model for cohesive fracture
998 Clemens. *International* 1102–1119. <https://doi.org/10.1002/nme>

999 Ren, H.L., Zhuang, X.Y., Anitescu, C., Rabczuk, T., 2019. An explicit phase field
1000 method for brittle dynamic fracture. *Comput. Struct.* 217, 45–56.
1001 <https://doi.org/10.1016/j.compstruc.2019.03.005>

1002 Salih, S., Davey, K., Zou, Z., 2016. Rate-dependent elastic and elasto-plastic cohesive
1003 zone models for dynamic crack propagation. *Int. J. Solids Struct.* 90, 95–115.
1004 <https://doi.org/10.1016/j.ijsolstr.2016.04.002>

1005 Samaniego, E., Anitescu, C., Goswami, S., Nguyen-Thanh, V.M., Guo, H., Hamdia,
1006 K., Zhuang, X., Rabczuk, T., 2020. An energy approach to the solution of partial
1007 differential equations in computational mechanics via machine learning:
1008 Concepts, implementation and applications. *Comput. Methods Appl. Mech. Eng.*
1009 362, 112790. <https://doi.org/10.1016/j.cma.2019.112790>

1010 Schillinger, D., Borden, M.J., Stolarski, H.K., 2015. Isogeometric collocation for
1011 phase-field fracture models. *Comput. Methods Appl. Mech. Eng.* 284, 583–610.
1012 <https://doi.org/10.1016/j.cma.2014.09.032>

1013 Silling, S.A., 2000. Reformulation of elasticity theory for discontinuities and long-
1014 range forces. *J. Mech. Phys. Solids* 48, 175–209. [https://doi.org/10.1016/S0022-5096\(99\)00029-0](https://doi.org/10.1016/S0022-5096(99)00029-0)

1015

1016 Silling, S.A., Epton, M., Weckner, O., Xu, J., Askari, E., 2007. Peridynamic states
1017 and constitutive modeling, *Journal of Elasticity*. <https://doi.org/10.1007/s10659-007-9125-1>

1018

1019 Song, X., Khalili, N., 2019. A peridynamics model for strain localization analysis of
1020 geomaterials. *Int. J. Numer. Anal. Methods Geomech.* 43, 77–96.
1021 <https://doi.org/10.1002/nag.2854>

1022 Song, X., Menon, S., 2019. Modeling of chemo-hydromechanical behavior of
1023 unsaturated porous media: a nonlocal approach based on integral equations. *Acta*
1024 *Geotech.* 14, 727–747. <https://doi.org/10.1007/s11440-018-0679-9>

1025 Song, X., Silling, S.A., 2020. On the peridynamic effective force state and multiphase
1026 constitutive correspondence principle. *J. Mech. Phys. Solids* 145, 104161.
1027 <https://doi.org/10.1016/j.jmps.2020.104161>

1028 Suchorzewski, J., Tejchman, J., Nitka, M., 2018. Discrete element method simulations
1029 of fracture in concrete under uniaxial compression based on its real internal
1030 structure. *Int. J. Damage Mech.* 27, 578–607.
1031 <https://doi.org/10.1177/1056789517690915>

1032 Tang, H., Zhu, F., Yang, D., Papazafeiropoulos, G., 2021. Numerical simulation of
1033 strain localization based on Cosserat continuum theory and isogeometric
1034 analysis. *Comput. Geotech.* 129, 103874.
1035 <https://doi.org/10.1016/j.compgeo.2020.103874>

1036 Vázquez, R., 2016. A new design for the implementation of isogeometric analysis in
1037 Octave and Matlab: GeoPDEs 3.0. *Comput. Math. with Appl.* 72, 523–554.
1038 <https://doi.org/10.1016/j.camwa.2016.05.010>

1039 Vuong, A. V., Giannelli, C., Jüttler, B., Simeon, B., 2011. A hierarchical approach to
1040 adaptive local refinement in isogeometric analysis. *Comput. Methods Appl.*
1041 *Mech. Eng.* <https://doi.org/10.1016/j.cma.2011.09.004>

1042 Wang, Y., Han, F., Lubineau, G., 2021. Strength-induced peridynamic modeling and
1043 simulation of fractures in brittle materials. *Comput. Methods Appl. Mech. Eng.*
1044 374, 113558. <https://doi.org/10.1016/j.cma.2020.113558>

1045 Wu, J.-Y., Nguyen, V.P., Nguyen, C.T., Sutula, D., Sinaie, S., Bordas, S.P.A., 2020.
1046 Chapter One - Phase-field modeling of fracture, in: Bordas, S.P.A., Balint,
1047 D.S.B.T.-A. in A.M. (Eds.), . Elsevier, pp. 1–183.
1048 <https://doi.org/https://doi.org/10.1016/bs.aams.2019.08.001>

1049 Yu, F., Wei, Y., Ji, Y., Chen, L.Q., 2018. Phase field modeling of solidification
1050 microstructure evolution during welding. *J. Mater. Process. Technol.* 255, 285–
1051 293. <https://doi.org/10.1016/j.jmatprotec.2017.12.007>

1052 Zhang, P., Yao, W., Hu, X., Zhuang, X., 2021. Phase field modelling of progressive
1053 failure in composites combined with cohesive element with an explicit scheme.
1054 *Compos. Struct.* 262, 113353. <https://doi.org/10.1016/j.compstruct.2020.113353>

1055 Zhang, X., Sloan, S.W., Vignes, C., Sheng, D., 2017a. A modification of the phase-
1056 field model for mixed mode crack propagation in rock-like materials. *Comput.*
1057 *Methods Appl. Mech. Eng.* 322, 123–136.
1058 <https://doi.org/10.1016/j.cma.2017.04.028>

1059 Zhang, X., Vignes, C., Sloan, S.W., Sheng, D., 2017b. Numerical evaluation of the
1060 phase-field model for brittle fracture with emphasis on the length scale. *Comput.*
1061 *Mech.* 59, 737–752. <https://doi.org/10.1007/s00466-017-1373-8>

1062 Zhou, S., Zhuang, X., Zhu, H., Rabczuk, T., 2018. Phase field modelling of crack
1063 propagation, branching and coalescence in rocks. *Theor. Appl. Fract. Mech.* 96,
1064 174–192. <https://doi.org/10.1016/j.tafmec.2018.04.011>

1065 Zhou, X., Wang, L., Shou, Y., 2020. Understanding the fracture mechanism of ring
1066 Brazilian disc specimens by the phase field method. *Int. J. Fract.* 226, 17–43.
1067 <https://doi.org/10.1007/s10704-020-00476-w>

1068 Zhu, F., Tang, H., Zhang, X., Li, Y., Papazafeiropoulos, G., 2021. An isogeometric
1069 approach to Biot-Cosserat continuum for simulating dynamic strain localization
1070 in saturated soils. *Comput. Geotech.* 133, 104036.
1071 <https://doi.org/10.1016/j.compgeo.2021.104036>

1072 Zhu, F., Zhao, J., 2021. Peridynamic modelling of blasting induced rock fractures. *J.*
1073 *Mech. Phys. Solids* 153, 104469. <https://doi.org/10.1016/j.jmps.2021.104469>

1074